A rheological constitutive model to predict the anisotropic biaxial bending behavior of spiral strands subjected to variable axial force

Mohammad Ali Saadat, Damien Durville

International Journal of Solids and Structures 305 (2024) 113082

Contents lists available at ScienceDirect

International Journal of Solids and Structures

journal homepage: www.elsevier.com/locate/ijsolstr

A rheological constitutive model to predict the anisotropic biaxial bending behavior of spiral strands subjected to variable axial force

Mohammad Ali Saadat *, Damien Durville

Université Paris-Saclay, CentraleSupélec, ENS Paris-Saclay, CNRS, LMPS - Laboratoire de Mécanique Paris-Saclay, 3 rue Joliot-Curie, Gif-sur-Yvette, 91190, France

ARTICLE INFO

Keywords:
Rheological model
Constitutive model
Biaxial bending
Anisotropic behavior
Variable axial force
Spiral strand

ABSTRACT

Spiral strands exhibit dissipative bending behavior when subjected to external axial force. To the best of the authors' knowledge, only the uniaxial bending behavior of spiral strands subjected to constant axial force has been studied in the literature so far. Thanks to a recently developed mixed stress–strain driven computational homogenization for spiral strands, this paper is the first to study the biaxial bending behavior of spiral strands subjected to variable tensile force. Based on the observed anisotropic behavior, a rheological constitutive model equivalent to multilayer spiral strands is proposed to predict their behavior under such loading. For an N_l-layer strand, the proposed model consists of several angularly distributed uniaxial spring systems, referred to as a multiaxial spring system, where each uniaxial spring system consists of a spring and N_l slider-springs. In a uniaxial spring system, the spring represents the slip contribution of all wires to the bending stiffness of the strand, while each slider-spring represents the stick contribution of each layer. A major advantage of the proposed scheme is its straightforward parameter identification, requiring only several monotonic uniaxial bendings under constant axial force. The proposed rheological model has been verified against the responses obtained from the mixed stress–strain driven computational homogenization through several numerical examples. These examples consist of complex uniaxial and biaxial load cases with variable tensile force. It has been shown that the proposed scheme not only predicts the response of the strand, but also provides helpful insight into the complex underlying mechanism of spiral strands. Furthermore, the low computational cost of the proposed models makes them perfect candidates for implementation as a constitutive law in a beam model. Using a single beam with the proposed constitutive law, spiral strand simulations can be performed in a few seconds on a laptop instead of a few hours or days on a supercomputer.

1. Introduction

A spiral strand is a multilayer composite of helically twisted wires, whose mechanical behavior has been extensively covered in the literature. Fig. 1 shows the cross-section and side view of a typical three-layer spiral strand. The ith layer of a spiral strand is characterized by the number of wires in the layer, n_i, the wire radius, R_i, and the lay angle, α_i. Spiral strands exhibit axial–torsional and axial-bending coupling due to the helical geometry of their constituent wires. In the case where the wires remain in the linear elastic regime, the axial–torsional behavior is linear, whereas, the bending behavior is nonlinear, only due to the frictional contact interaction between different layers. The methods developed to model the bending behavior of spiral strands can be divided into three general categories, namely, macroscopic, microscopic, and microscopic–macroscopic (multiscale) approaches.

In the macroscopic approach, the behavior of a strand cross-section, namely the moment–curvature response, is characterized, which can then be used in a beam element to model the macroscopic behavior of a strand in different configurations. The main advantage of this approach is its low computational cost since a single beam represents the spiral strand. However, this approach faces difficulties and limitations, as thus far, only analytical formulations have been used to define the cross-section behavior, and due to the complex geometry of spiral strands and their underlying mechanisms, only simple strands could be modeled. The analytical approaches can be broadly divided into two categories, namely, discrete and semi-continuous formulations. In the discrete formulation, each wire is considered individually, while in the semi-continuous formulation, each layer of the strand is considered as a homogeneous hollow cylinder.

Early attempts using the discrete formulation, such as Costello (1997), Costello and Butson (1982) and LeClair and Costello (1988), neglected interlayer friction and calculated the bending stiffness as the sum of the individual wire stiffnesses, making them valid only in the

* Corresponding author.
E-mail address: mohammad-ali.saadat@centralesupelec.fr (M.A. Saadat).

https://doi.org/10.1016/j.ijsolstr.2024.113082
Received 13 June 2024; Received in revised form 10 August 2024; Accepted 19 September 2024
Available online 24 September 2024

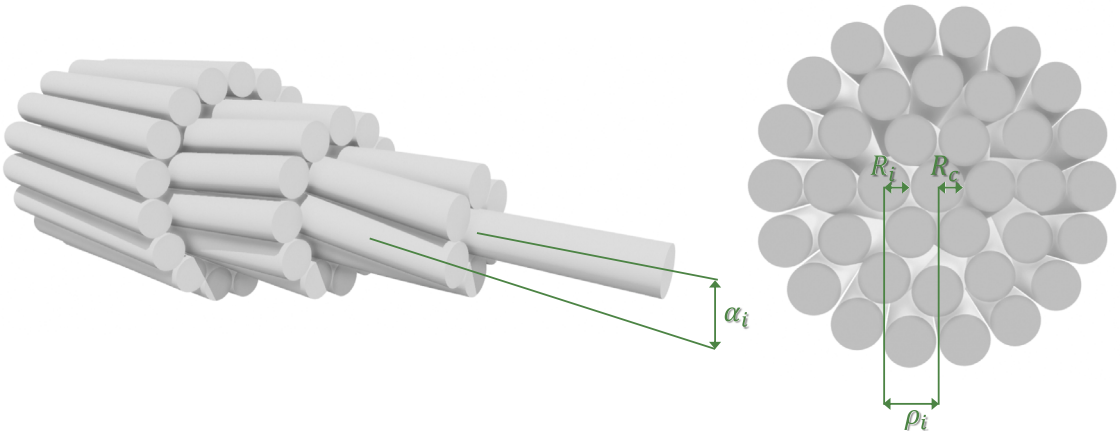

Fig. 1. The side view, internal configuration and cross section of a typical three-layer spiral strand.

absence of axial force. Initial models including friction assumed binary states: no friction (minimum stiffness) or infinite friction (maximum stiffness) (Ramsey, 1988). For infinite friction, bending moments result from individual wire bending and axial force variation due to friction. In Lanteigne (1985), interlayer friction is considered due to the external tensile force, causing bending stiffness to vary stepwise. As curvature increases in a taut spiral strand, slip progresses from the outermost to the innermost layer, identified by a stick–slip criterion. Papailiou (1995, 1997) used similar equations but allowed partial slip, resulting in a smooth transition in bending stiffness. This formulation provides a nonlinear bending response with good agreement with experimental results. Subsequent modifications include Dastous (2005), Inagaki et al. (2007), Hong et al. (2012), Paradis and Légeron (2011), Khan et al. (2018), Hong et al. (2005), Foti and Martinelli (2016a) and Zheng et al. (2021). In Hong et al. (2005), minimum stiffness depends on friction coefficient, while Dastous (2005) extended Papailiou's work to include nonlinearities and dynamic implementation. Khan et al. (2018) incorporated intralayer line contacts, and Foti and Martinelli (2016b) used Euler–Bernoulli beam theory to model each wire as a curved thin rod (Love, 1927). Vemula et al. (2020) developed a model for the elasto-plastic bending response of wires under large deflections.

For a complete review of available analytical models for spiral strands, refer to Utting and Jones (1984), Triantafyllou (1984), Starossek (1994), Cardou and Jolicoeur (1997) and Rega (2004a,b). Although these analytical approaches provide helpful insight into the behavior of these cables, they cannot address all the internal nonlinear mechanisms of complex strands.

A purely microscopic approach can overcome the deficiencies of the macroscopic approach by explicitly modeling all cable constituents, including wires and frictional contact interactions, using the finite element (FE) method. Despite its high accuracy and ability to model complex geometries, this approach's high computational cost limits its application to short samples of small strands. Various elements, from 3D solid to 1D beam elements, can be used. These FE simulations, referred to as direct numerical simulations (DNS), include full 3D FE simulations for modeling spiral strands (Kmet et al., 2013; Zhang and Ostoja-Starzewski, 2016; Yu et al., 2014). To reduce computational costs, concise FE models (Jiang, 2012) and simplified models with beams and springs (Yu et al., 2016) have been proposed.

Taking advantage of the slenderness of the wires, they can be modeled using 1D beam elements, which has the advantage of reducing the computational cost. However, this choice introduces two difficulties in modeling the spiral strands. The first is selecting the appropriate beam element to use, and the second is dealing with beam-to-beam contact, which is more difficult to address than contact between 3D deformable bodies.

To model highly flexible structures, various beam elements have been used. Kirchhoff-type models are suitable for very slender beams with insignificant axial deformation and transverse shear (Love, 1927; Meier et al., 2015). General cases consider shear deformation, leading to coupled equations for position and rotation (Reissner, 1973; Simo, 1985), requiring methods like rotation parameterization (Cardona and Geradin, 1988; Crisfield and Jelenić, 1999; Ghosh and Roy, 2009), the director vector method (Simo, 1985), and Lie group methods (Betsch and Steinmann, 2002; Brüls et al., 2012). Challenges include objectivity issues and singularities. A beam formulation on the $SE(3)$ manifold couples rotational and translational degrees of freedom (Sonneville et al., 2014). Assuming variable section directors capture beam deformation without rotation variables (Durville, 1998), and higher-order beam elements can represent complex deformations (Moustacas et al., 2021).

Two types of interwire contact can occur in a spiral strand: line contact between the core and the wires of the first layer and between the wires of the same layer, and point contact between the wires of different layers. Contact mechanics between 3D bodies has been the subject of extensive research (see for example Wriggers and Laursen, 2006). However, due to the particular geometric properties of beams, the contact treatment can be more challenging and scarce. The contact constraint in the case of beam-to-beam contact is generally defined by the closest point projection and enforced using the Lagrange multiplier method or the penalty approach (Wriggers and Zavarise, 1997; Zavarise and Wriggers, 2000). These papers considered point-to-point contact. More recently, the mortar method has been implemented in the case of frictionless quasi-static beam-to-beam contact (Bosten et al., 2022; Tomec and Jelenić, 2022) for the case of line contact. In Meier et al. (2018) both cases of point-to-point and line contact have been considered and a switch between the two models has been presented. In Durville (2012), the contact has been considered as a phenomenon involving the two structures in contact symmetrically with respect to an intermediate geometry, and even though the contact is considered point by point, the use of a large number of contact points allows the modeling of line contact.

Although beam elements have been successfully used in several applications (Durville, 2012, 2010, 2005), they have rarely been used to model spiral strands (Zhou and Tian, 2013; Lalonde et al., 2017b,a; Ménard and Cartraud, 2021; Kim et al., 2021; Kim and Lee, 2017; Yu et al., 2018; Baumann and Novak, 2017; Beleznai and Páczelt, 2013; Zhou et al., 2022). In Zhou and Tian (2013), a single-layer strand has been modeled using beam elements, however, since wire slippage has not been considered in this work, it cannot be used for bending simulation. In Kim and Lee (2017), the performance of beam elements in modeling spiral strands has been compared to 3D elements, for torque balance design of several spiral strands. It has been shown that

the use of beam elements in numerical simulation of these cables provides high accuracy, while the computational cost is lower. The work of Lalonde et al. (2017b), can be considered as the first attempt to fully utilize the beam elements to model the mechanical behavior of spiral strands, as this is the first paper that deals with the complex situation of nonlinear bending behavior of spiral strands when subjected to axial force using beam elements. In this work, the bending responses of two cables previously used experimentally in Papailiou (1995) have been studied, and good agreement has been found. Using the same modeling strategy, the authors have investigated the fatigue analysis for an overhead conductor in Lalonde et al. (2017a). Due to the high accuracy of the stresses, strains and the contact forces obtained from numerical simulation compared to analytical approaches, the results are more accurate and reliable. In Beleznai and Páczelt (2013), the axial bending response of an Aluminum Conductor Steel Reinforced (ACSR) cable has been verified against experimental results. Although using beam elements would reduce the computational cost compared to full 3D simulations, modeling large samples of large cables is still out of reach. In this case, multiscale simulation becomes an option.

Even though the above models provide accurate results, their computational cost is too high for modeling samples of reasonable lengths for bending. Therefore, an alternative approach, such as the multiscale approach, should be used. Multiscale modeling predicts a structure's behavior involving multiple scales, using homogenization methods for clearly separated scales and concurrent methods for coupled scales. Homogenization replaces a heterogeneous medium with an equivalent homogeneous one derived from a micro-sample. For spiral strands, the heterogeneous medium is the strand of many wires, and the homogeneous medium is a single beam. A representative volume element (RVE) must be large enough to represent the heterogeneity's randomness and have homogenized properties insensitive to its size. Homogenization methods include analytical homogenization, such as the semi-continuous formulation for spiral strands, and computational homogenization.

In the computational homogenization framework, the macroscopic constitutive behavior is characterized numerically, from solving a boundary value problem (BVP) on the RVE scale. Therefore, no explicit a priori assumption on the macroscopic constitutive behavior is required, which makes the method extremely flexible and suitable for predicting very complex nonlinear behaviors. In conventional strain-driven computational homogenization at finite strain, after discretizing the macroscopic domain, the macroscopic deformation gradient is computed for each integration point. This deformation gradient is then imposed on the RVE using appropriate boundary conditions. After solving the BVP on the RVE, the resulting macroscopic stresses and the macroscopic consistent tangent modulus are retrieved and assigned to the integration point for the next iteration of the macroscopic BVP. For a complete review of the multiscale modeling, refer to Matouš et al. (2017).

Due to the quasi-invariance of phenomena along the axis of spiral strands, homogenization can be applied to these structures. Various attempts at homogenizing beam-like structures have been made in the literature (Treyssede and Cartraud, 2022; Staszak et al., 2022; Xing et al., 2022; Boso et al., 2005; Buannic and Cartraud, 2001; Bussolati, 2019; Ménard and Cartraud, 2021; Cartraud and Messager, 2006; Karathanasopoulos and Kress, 2016; Frikha et al., 2013; Smith et al., 2023; Saadat and Durville, 2023). In Karathanasopoulos and Kress (2016) and Frikha et al. (2013), a two-dimensional homogenization scheme is proposed by reducing the 3D microscopic problem to a 2D finite element simulation on the cross-section, with axial and torsional loading considered but not bending. In Treyssede and Cartraud (2022), this is addressed by accounting for the dependence on the axial coordinate, enabling the modeling of bending behavior. In Ménard and Cartraud (2021), asymptotic homogenization previously developed in Cartraud and Messager (2006) is extended to consider contact nonlinearities, capturing the nonlinear bending response of strands accurately and at low computational cost, with detailed wire stress and contact force information provided. In Saadat and Durville (2023), a mixed stress–strain driven computational homogenization for spiral strands is developed using a geometrically exact beam element (Cardona and Geradin, 1988) for the macroscale and a kinematically enriched beam element (Durville, 1998) for the microscale. The mixed stress–strain driven approach developed allows either force or deformation to be used to drive the problem. Recently, in Smith et al. (2023), a repeated unit cell finite element approach for spiral strands is developed using 3D solid elements for individual wires and a constant curvature constraint for bending curvature.

In all of the above studies, the focus has been on identifying the nonlinear uniaxial bending response of a spiral strand subjected to a constant tensile force, and except in Saadat and Durville (2023), no integration of the responses in a full homogenization scheme has been performed. In this study, it has been shown that since the axial–torsional response of spiral strands can be assumed to be linear, if the nonlinear evolution of the uniaxial bending response as a function of curvature history can be predicted, there is be no need to perform FE^2 (Feyel and Chaboche, 2000) homogenization, which is computationally intensive. As an alternative, an interpolation technique has been introduced to obtain the uniaxial cyclic response of spiral strands subjected to a constant axial force for any curvature history from only a monotonic response in order to evaluate the bending stiffness at any point, thus allowing a full homogenization to be performed without having to solve an RVE BVP at each macroscopic interpolation point. By comparing the results obtained by performing full homogenization with DNS, good agreement has been observed along with a significant reduction in computational time. The main conclusions that can be drawn from this study are, firstly, that a spiral strand can be replaced by a single beam with equivalent material properties, and secondly, that by considering the axial–torsional coupling as linear, the bending response for the beam is the only nonlinear term which needs to be predicted.

To the best of the author's knowledge, spiral strand models in the literature consider only uniaxial bending of spiral strands subjected to constant tensile force, whereas in reality these strands are usually subjected to biaxial bending and variable tensile force. Therefore, using the conclusions that can be drawn from Saadat and Durville (2023), the objective of this paper is to present a rheological constitutive model for spiral strands that is able to describe the biaxial bending behavior of spiral strands subjected to variable axial force. The proposed rheological constitutive model consists of a combination of basic rheological elements, i.e. springs and slider elements. A notable advantage of this model is that it involves only a few parameters, all of which have direct physical interpretations and can be easily obtained from several monotonic uniaxial bending tests under constant tensile force. In addition, the model has a very low computational cost, which allows it to be used as a constitutive law for a beam model. Although no experiments have apparently yet been performed on spiral strands subjected to biaxial bending or variable tensile force, the homogenization framework developed in Saadat and Durville (2023) enables performing virtual experiments with low computational cost to characterize the response of a spiral strand subjected to these conditions. For this reason, in the absence of available experimental results, the rheological model will be verified only against results obtained by solving the BVP on the RVE. This is due to the fact that in Saadat and Durville (2023), the mixed stress–strain driven homogenization has already been validated against DNS, which itself has been verified against experimental data in the literature.

This paper is organized as follows. First, an introduction to mixed stress–strain homogenization of spiral strands is presented, which is used to extract their moment curvature responses. Next, using the homogenization method, the bending behavior of spiral strands subjected to different loadings is extracted and presented. Then, the rheological model capable of predicting the uniaxial bending of spiral strands subjected to variable axial force is presented, followed by the rheological

model for predicting the biaxial bending response under variable tensile force. Then, the accuracy and robustness of the proposed framework is illustrated through some numerical examples. Finally, some concluding remarks are given.

2. The mixed stress–strain driven computational homogenization for spiral strands

To extract the moment curvature response of spiral strands, the mixed stress–strain driven computational homogenization developed in Saadat and Durville (2023) is implemented in an in-house finite element code. In Saadat and Durville (2023), beam kinematics at the macroscale have been assumed, allowing homogenization to be performed only in the longitudinal direction. Additionally, a quasi-periodic boundary condition has been introduced by modifying the Hill–Mandel macrohomogeneity condition, which enables homogenization on non-periodic RVEs. The final system of equations to be solved is:

$$\begin{pmatrix} \frac{1}{L_{\mathrm{RVE}}}\frac{\partial^2 W^m}{\partial \boldsymbol{u}^{m2}} & \mathbf{A}_P^T & \mathbf{0} \\ \mathbf{A}_P & \mathbf{0} & -\mathbf{A}_P \frac{\partial \hat{\boldsymbol{u}}_M^m}{\partial \hat{\boldsymbol{E}}^M} \\ \mathbf{0} & -\left(\mathbf{A}_P \frac{\partial \hat{\boldsymbol{u}}_M^m}{\partial \hat{\boldsymbol{E}}^M}\right)^T & -\hat{\boldsymbol{\lambda}}^T \mathbf{A}_P \frac{\partial^2 \hat{\boldsymbol{u}}_M^m}{\partial \hat{\boldsymbol{E}}^{M2}} \end{pmatrix} \begin{pmatrix} \delta \boldsymbol{u}^m \\ \delta \hat{\boldsymbol{\lambda}} \\ \delta \hat{\boldsymbol{E}}^M \end{pmatrix} = \begin{pmatrix} -\frac{1}{L_{\mathrm{RVE}}}\frac{\partial W^m}{\partial \boldsymbol{u}^m} - \hat{\boldsymbol{\lambda}}^T \mathbf{A}_P \\ -\mathbf{A}_P\left(\hat{\boldsymbol{u}}^m - \hat{\boldsymbol{u}}_M^m\right) \\ \hat{\boldsymbol{S}}^M + \hat{\boldsymbol{\lambda}}^T \mathbf{A}_P \frac{\partial \hat{\boldsymbol{u}}_M^m}{\partial \hat{\boldsymbol{E}}^M} \end{pmatrix}, \tag{1}$$

here, L_{RVE} denotes the length of the RVE, and W^m represents the work within the RVE. The term $\boldsymbol{u}^m$ indicates the total microscopic displacement field, while $\boldsymbol{u}_M^m$ is the microscopic displacement field induced by macroscopic strains $\hat{\boldsymbol{E}}^M = [\epsilon, \kappa_x, \kappa_y, \kappa_z]$, where ϵ is the axial strain, κ_x and κ_y are two bending curvatures and κ_z is the twist. The matrix $\mathbf{A}_p$ relates the degrees of freedom of the opposite faces of the RVE. The vector $\hat{\lambda}$ contains the Lagrange multipliers that enforce the quasi-periodic boundary conditions. Lastly, $\hat{\boldsymbol{S}}^M = [T, M_x, M_y, M_z]$ represents the vector of macroscopic resultant forces and moments which includes an axial force, T, torque, M_z, and two bending moments M_x and M_y. It should be mentioned that geometric nonlinearities have been completely taken into account in the microscale.

Due to the mixed stress–strain formulation, the macroscopic strains $\hat{\boldsymbol{E}}^M$ enter the RVE BVP as displacement degrees of freedom, while $\hat{\boldsymbol{S}}^M$ are their corresponding forces, as can be seen in Eq. (1). Therefore, the degrees of freedom corresponding to macroscopic strains and their associated resultant forces and moments are treated as conventional displacement and forces in the finite element setting.

The computational homogenization developed in Saadat and Durville (2023) serves us in two ways. First, it provides the mathematical proof that a spiral strand can be replaced by a single beam with effective material properties. Second, it provides a virtual experimental platform for spiral strands to determine their response to any arbitrary loading history for any strand geometry with minimal computational effort.

3. The bending behavior of spiral strands

To develop a rheological model capable of predicting the bending behavior of spiral strands, an in-depth analysis of this behavior is essential. To this end, we investigate the behavior of three spiral strands (Fig. 2), with geometric properties in Table 1, under different loadings by solving Eq. (1). These loadings consist of both uniaxial cyclic bending under constant and variable tensile forces, and biaxial bending under constant tensile force. The findings from this section will be used in the development of the rheological model that can predict biaxial bending under variable tensile force.

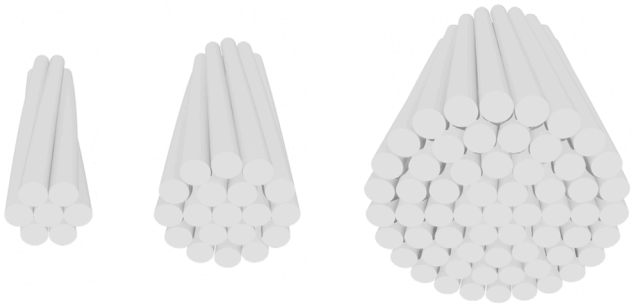

Fig. 2. The representative volume elements of a single-, two-, and four-layer strand.

Table 1
Geometric properties of the spiral strands.

	No. of wires	Radius [mm]	Pitch length [mm]
Single-layer			
Core	1	2.675	–
Layer 1	6	2.590	230.1
i-layer			
Core	1	2.675	–
Layer i	$6\times i$	2.590	$228.44\times i$

In all cases, the friction coefficient of 0.3 and the Young's modulus of 210 GPa have been assumed in the numerical simulation. Moreover, the contact regularization parameters (Saadat and Durville, 2023) of 10^{-4} mm for the single-layer strand, and 10^{-3} mm for the two- and four-layer strands have been considered in the numerical simulations.

3.1. Uniaxial bending under constant tensile force

The first loading considered is the most basic one: uniaxial bending under constant tensile force. The moment–curvature responses of the strands subjected to a cyclic bending with a curvature amplitude of $10^{-4}\mathrm{mm}^{-1}$ and different tensile stresses are shown in Fig. 3.

The observed strands show nonlinear dissipative behavior. To understand the reason of this nonlinear behavior, we consider the two-layer strand at different stages of loading. Initially, a tensile force is applied to the spiral strand, creating normal interlayer contact forces due to the strand's helical geometry, as shown in Fig. 4. Line contacts form between wires of the first layer and the core wire due to their continuous contact. However, point contacts occur between wires of the first and of the second layers due to their opposing lay directions.

Once the axial force is applied to the strand and these contacts have been made, the bending curvature is applied to the strand. When a bending curvature is applied to the strand, interlayer shear forces are induced and two extreme cases of relative interlayer displacement can be considered, namely, full-slip and full-stick. In the full-slip case, it is assumed that there are no induced interlayer shear forces and therefore each wire acts individually and bends around its own neutral axis, so the strand's bending stiffness is at its minimum value. The distribution of the axial strain induced by applying a bending curvature of κ under this assumption is shown schematically in Fig. 5(a) for a five-wire assembly. On the contrary, in the full-stick case, all the bending induced shear forces are transferred between the layers due to the presence of interlayer friction, and therefore, the cross section is considered to be rigid and the bending stiffness is at its maximum value. As a result, a linear variation of the bending induced axial strain in the cross section is considered. The distribution of the bending induced axial strain under the full-stick assumption is shown schematically in Fig. 5(b). Under the assumption of a linear variation of the induced axial strain, the axial strain across the cross section of each wire can be split into two components. One reflects a linear variation in the wire

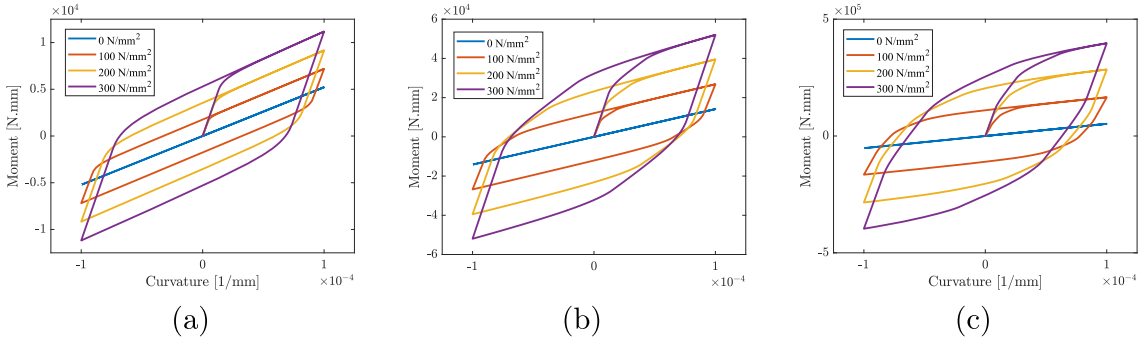

Fig. 3. The uniaxial cyclic bending responses of spiral strands subjected to different constant tensile stresses of 0, 100, 200 and 300 N/mm^2. a, the single-layer strand; b, the two-layer strand; c, the four-layer strand.

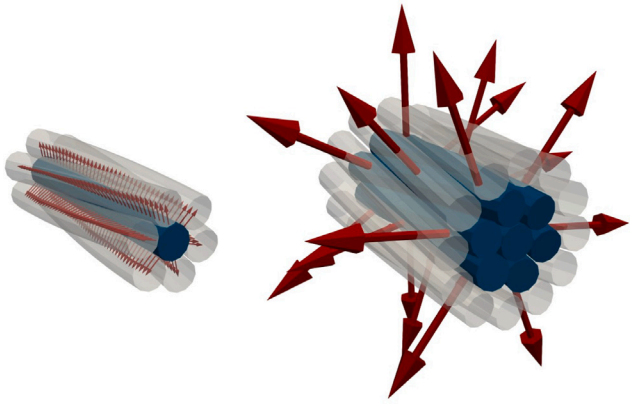

Fig. 4. The normal contact forces developed between different layers of a two-layer spiral strands when subjected to an external tensile force.

cross section independent of the wire's position within the cable cross section, while the other component is constant over each wire cross section but varies linearly with the distance from the centerline of the wire to the strand axis. Integrating the axial stresses associated with these two components to calculate the assembly bending moment gives rise to different bending stiffness terms, referred to in the following as the slip contribution and the stick contribution to the bending stiffness, respectively.

Using the above explanations, it is possible to calculate the minimum and maximum bending stiffnesses of the lth layer of a strand. Considering the full-slip case, the minimum bending stiffness is:

$$K_{\min,l} = K_{\text{slip},l} = n_l E_l \frac{\pi R_l^4}{4} cos\alpha_l, \tag{2}$$

where n_l is the number of wires, E_l is the Young's modulus of wires, R_l is the radius of wires, and α_l is the lay angle of the lth layer. To determine the stick contribution to the maximum bending stiffness, the axial forces of the wires are calculated under the full-stick assumption, as described previously. The maximum bending stiffness of the layer can then be expressed as Papailiou (1997) and Foti and Martinelli (2016b):

$$K_{\max,l} = K_{\min,l} + \beta \frac{n_l}{2} E_l A_l \rho_l^2 cos\alpha_l^3 = K_{\text{slip},l} + K_{\text{stick},l}, \tag{3}$$

where ρ_l is the helix radius of the layer. The coefficient β has been considered here to account for the possibility of incomplete load transfer, especially for the wires with pointwise interlayer contacts and those that are not fully supported by the underlying layer. Note that this factor has not been taken into account in the previous studies, for example in Papailiou (1997) and Foti and Martinelli (2016b).

In the above expressions, the slip contribution to the bending stiffness $K_{\text{slip},l}$ corresponds to the sum of the bending stiffnesses of all wires of the layer, and is always present, whereas the stick contribution $K_{\text{stick},l}$ vanishes once the slip has occurred. In the same way, the bending moment of a layer is split into a slip contribution, varying linearly with the curvature, and a stick contribution, which is limited by the value reached at slipping.

In order to explain the nearly multilinear behavior observed in Fig. 3, the bending stiffness of the two-layer strand is examined at different stages of loading. At low curvatures, the interlayer friction is high enough to transfer the bending induced interlayer shear forces between different layers, and therefore both the first and second layers contribute to the overall bending stiffness of the strand with both slip and stick contributions. However, as the curvature increases, slip occurs between the first and second layers, resulting in the loss of the second layer's stick contribution to the bending stiffness, which is reflected by the change in the slope of the moment–curvature diagram. At this point, the second layer's stick contribution to the bending moment no longer increases, and reaches a maximum value which is referred to as the layer's slip moment threshold. As the curvature increases further, a second slip occurs between the first layer and the core wire, resulting in the loss of the first layer's stick contribution to the bending stiffness. At this point, the total bending stiffness of the strand is reduced to the sum of the slip contributions of the first and second layers, and

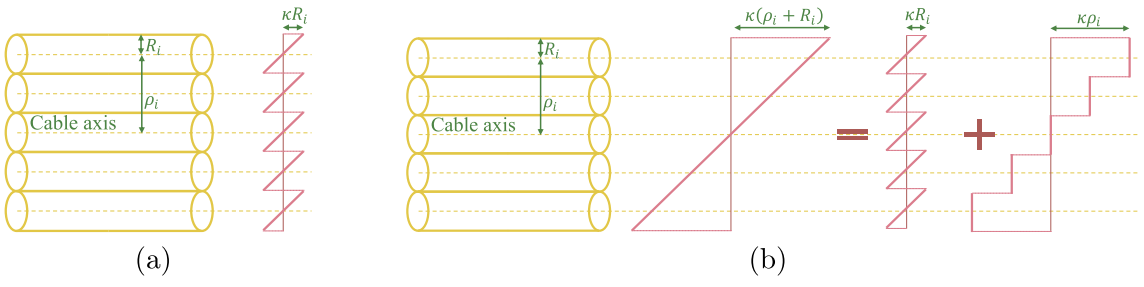

Fig. 5. Axial strain distribution for a five-wire assembly under different bending assumptions when subjected to a bending curvature κ. a, the full-slip assumption; b, the full-stick assumption.

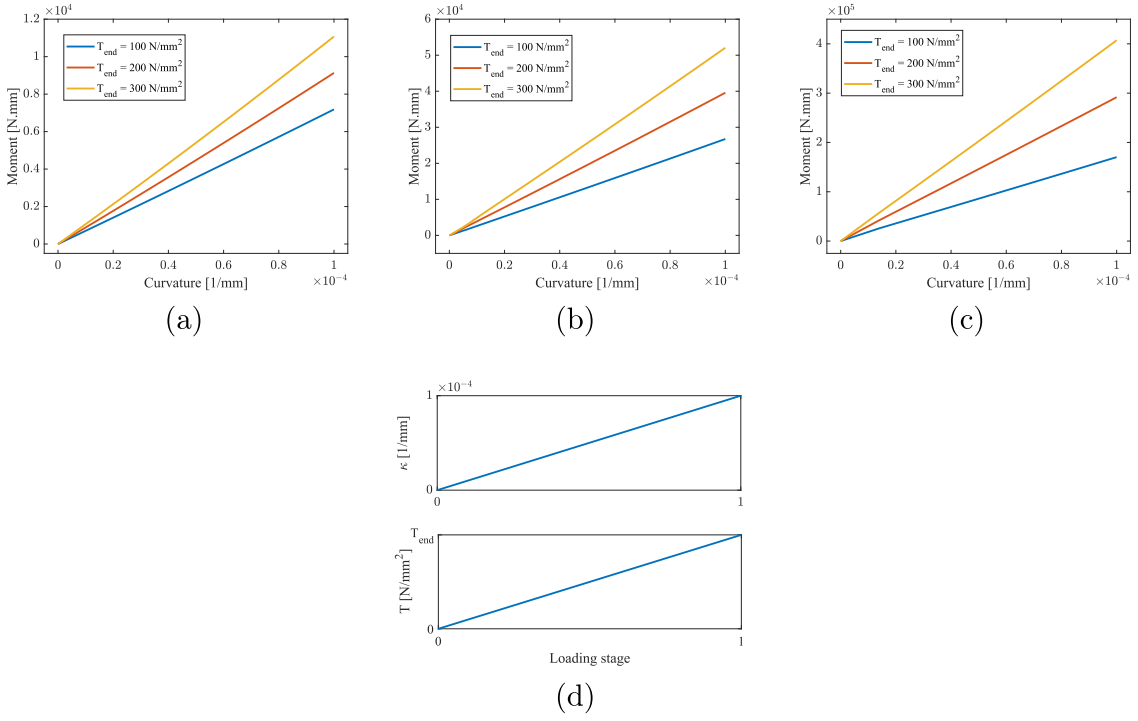

Fig. 6. The uniaxial bending responses of spiral strands obtained from homogenization under increasing curvature and tensile force. a, the single-layer strand; b, the two-layer strand; c, the four-layer strand; d, the loading history.

the core wire. The same pattern exists for different values of the axial force for the two-layer strand, only the slip between different layers occurs at different curvatures. Therefore, it can be concluded that the slip threshold of the layers is a function of the applied axial force. The uniaxial bending behavior of the single- and four-layer strands can be explained in the same way, as shown in Fig. 3. In general, for an N_l-layer strand under uniaxial bending and constant axial force, the slip starts from the outermost layer, i.e., between layers N_l and N_{l-1}, and propagates inwards, with the final slip occurring between the first layer and the core wire.

3.2. Uniaxial bending under variable tensile force

The purpose of this section is to illustrate, using two special load cases, very different behaviors that can be observed in the presence of a variable tensile load. Uniaxial bending is considered to isolate the effect of axial force variation. The two load cases examined here show opposite variations of the axial force with respect to the curvature, depending on whether the axial force increases (first case) or decreases (second case) linearly with the curvature. The moment–curvature responses obtained from homogenization, as well as their corresponding loading histories, are depicted in Figs. 6 and 7.

The axial force significantly affects the bending response of spiral strands, as demonstrated by these loads. Depending on whether the axial load is increasing or decreasing with the curvature, an almost linear response with varying slopes or even a softening response can be observed (Figs. 6 and 7), instead of the multilinear response obtained with constant axial force (Fig. 3). The observed almost linear response with increasing axial force can be explained by the nearly linear relationship between the interlayer normal contact forces and the applied axial force. Therefore, as the axial force increases, the normal contact force and thus the interlayer slip threshold increase almost linearly. In this load case, the bending induced interlayer shear appears to remain greater than the resisting interlayer frictional forces at all load steps, and therefore the layers are always in the slip state. However, due to the linear increase of axial force, the slip moment thresholds of all layers also increase almost linearly. Therefore, at each step, the moment of the strand is equal to the sum of the slip moment thresholds of all layers plus the slip contributions of all layers, all of which are almost linear, explaining the observed almost linear behavior of the strand. The fact that the bending moment in the last step of loading is equal to the case with constant tensile force (Fig. 3), supports the validity of the explanation provided for the observed behavior.

For the decreasing axial force case, the mechanism is similar to the constant axial force case, except that the slip thresholds of the layers are not constant but decrease linearly with the curvature. Therefore, the interlayer friction is initially high enough to prevent slipping and high bending stiffness can be observed for all samples. However, unlike the case with constant axial force, once a layer has slipped and its contribution to the bending stiffness has been lost, its slip moment threshold does not remain constant but decreases linearly. Since two different competing mechanisms contribute to the resulting bending moment of the strand after all layers have slipped, different behaviors can be observed. The first mechanism is reflected in the increase in the slip contribution of all wires to the bending moment, while the second mechanism is related to the decrease in the slip moment threshold of all layers. In some cases, such as the single-layer strand with $T_0 = 100$ N/mm^2, the increasing mechanism is stronger and therefore no softening is observed, whereas for all cases with the four-layer strand, a strong softening behavior can be observed. The fact that the bending moment in the last step of loading is the same in all cases, and is equal to the case where no tensile force has been applied to the strand (Fig. 3), confirms the validity of the explanation provided for the observed behavior.

3.3. Biaxial bending under constant tensile force

The effect of biaxial bending on the behavior of spiral strands is investigated in the last load case considered here. To isolate the effect of biaxial bending, a constant axial force is assumed. As long as uniaxial bending has been considered, the bending loading has been defined by a single value, i.e. the applied curvature κ, assuming a constant

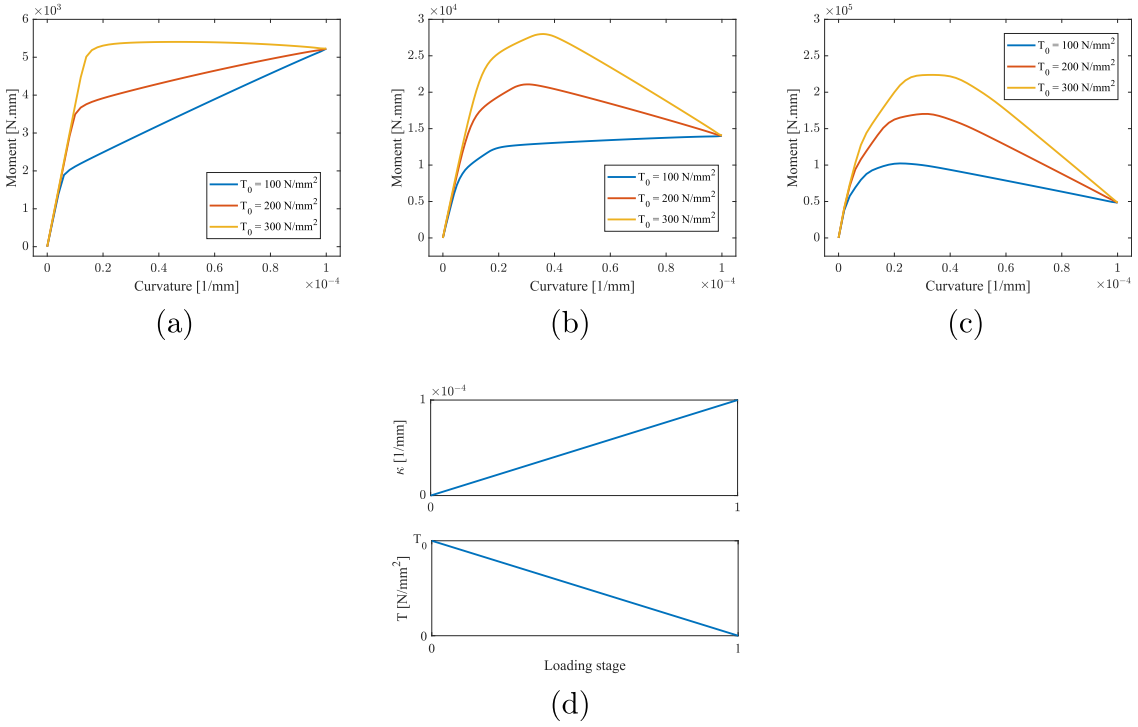

Fig. 7. The uniaxial bending response of spiral strands obtained from homogenization under increasing curvature and decreasing tensile force. a, the single-layer strand; b, the two-layer strand; c, the four-layer strand; d, the loading history.

bending direction. However, in the case of biaxial bending, the bending axis can be variable, and therefore two variables, namely the current increment of curvature and the current direction of the bending axis, are needed to define the bending load. Therefore, the applied curvature and consequently the bending moment should be treated as vectorial variables. Having the applied curvature and the bending moment as vectors, two different representations can be used to illustrate the results of biaxial bending of spiral strands; the x and y components of the vectors, or the amplitude of the vectors and their angle with respect to the x-axis.

Since the first representation is more convenient for defining the load history, it is used first. In this biaxial loading case, after performing a bending about the x-axis, the curvature in this direction is kept constant and a bending about the y-axis is performed. In the last stage, the curvature in y-axis is kept constant and the curvature in x-axis is further increased. This load history and the responses of the strands obtained by solving the BVP on the RVE are shown in Fig. 8.

Of great interest in this loading case is the anisotropic behavior induced in all strands. Spiral strands are radially symmetric in their initial state, but interlayer slip significantly affects their response in different directions. This effect has not yet been reported in the literature. To better understand this phenomenon, it is important to note that, contrary to the previous simplified presentation of the occurrence of interlayer slipping as an abrupt event when discussing the uniaxial response of strands, this interlayer slipping actually occurs gradually, as illustrated by the smooth transitions at changes in slope observed in the moment–curvature responses (see Fig. 3). The homogenization results can be used to follow the progression of the loss of stick contribution to the bending stiffness of each layer. For illustration, let us consider a single-layer strand subjected to a uniaxial bending about the x-axis and a tensile stress of 200 N/mm^2. In this case, the polar angles 0° and 180° define the bending neutral axis. As depicted in Fig. 9, which illustrates the occurrence of slipping for wires as function of their polar angle in the cross section and different loading steps, the points closest to the neutral axis start to slip and lose their stick contribution first. The slipping then propagates towards the two extreme angles, 90° and 270°, causing a loss of stick contribution to the bending stiffness, until the entire layer has lost its stick contribution to the bending stiffness. It should be noted that a wire located at the polar angle 90° experiences bending induced tension, and due to consideration of geometric nonlinearities in the numerical simulation, it loses its stick contribution later than a wire located at the angle 270°.

The curvature (or bending moment) at which the stick contribution to bending stiffness is lost in each direction can be considered as the history variable for that direction, since after this loss, the response in that direction is no longer linear due to the occurrence of slipping. The anisotropic response observed in Fig. 8 arises from the presence of distinct history variables in various directions, as illustrated in Fig. 9. When the bending axis changes, some directions continue to be loaded, while others are unloaded. The evolution of slipping in each direction, i.e. whether it starts, stops or continues, depends not only on the increment of curvature, but also on the slipping history in this direction. To capture the anisotropic response of the spiral strands, it is therefore necessary to capture and store the history variables in different directions. It is also interesting to note that the bending moment about the x-axis drops significantly in the response observed in Fig. 8 when the curvature is increased about the y-axis, which can be explained by a stress relaxation due to the triggering of slipping in some directions.

The responses of the strands using the second representation are depicted in Fig. 10. Comparing the total bending moment response to each of its components, no large jumps can be observed, and it appears that there is no difference between the biaxial and uniaxial responses except for a few small drops. However, the main difference between the two responses is revealed by looking at the axes of the applied curvature and the bending moment response. It can be observed that the two axes are aligned in the first loading stage, but as soon as the axis of applied curvature starts to vary, the two axes become misaligned, which means that the direction of applied curvature and bending moment are not the same, a result that has not been mentioned in the literature before.

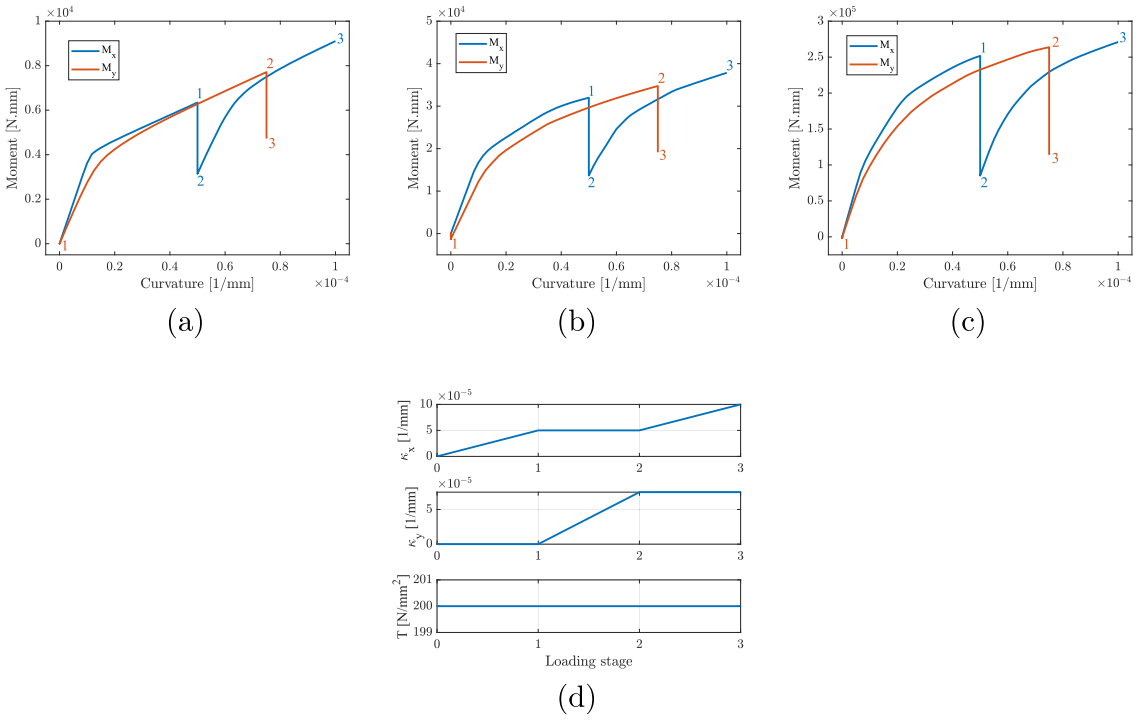

Fig. 8. The bending responses in the x- and y-axes of spiral strands obtained from homogenization under constant tensile force (the end of each load stage is marked on each curve). a, the single-layer strand; b, the two-layer strand; c, the four-layer strand; d, the loading history.

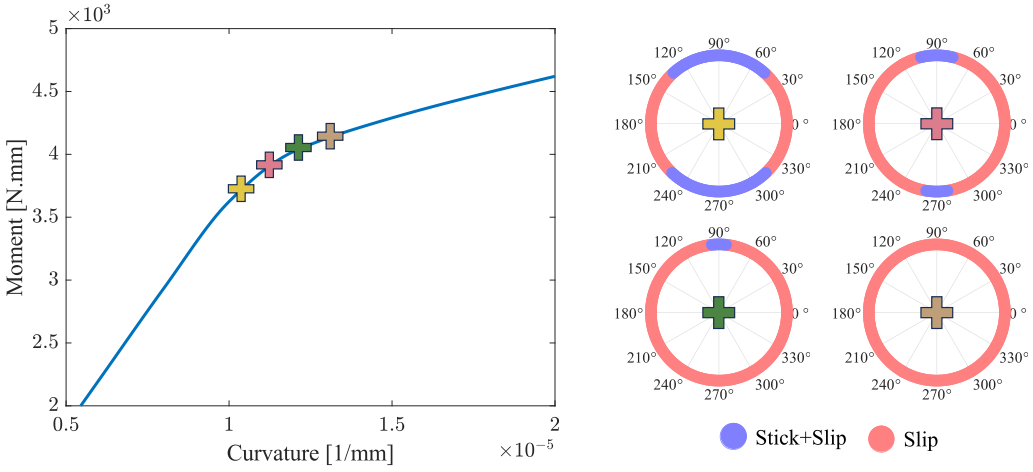

Fig. 9. Different contributions of a wire to the bending stiffness of a single-layer spiral strand subjected to uniaxial bending and constant axial force, at different polar angles in the cross section.

4. The uniaxial rheological model

The previous section demonstrated that simulations on short samples of spiral strands using computational homogenization can extract the bending response to different loadings. It has been observed that the variation of axial force has a significant impact on the bending response. The objective of this section is to present a rheological model that describes all the behaviors observed in the previous section.

Based on the uniaxial bending response of the strands subjected to a constant tensile force (Fig. 3), it is observed that this behavior resembles plasticity-like behavior with kinematic hardening. With this analogy, a rheological model based on springs and slider elements is proposed to reproduce this response. Fig. 11 illustrates these rheological elements and their constitutive behavior. In the context of bending of spiral strands, an analogy will be effectively drawn between the key parameters used and the traditional rheological elements. The moment experienced by a spiral strand during bending is analogous to stress in an elasto-plastic constitutive model. Similarly, curvature serves as an analogy to strain, bending stiffness can be compared to Young's modulus, and finally, the slip moment threshold corresponds to the yield stress. By adopting these analogous terms, for the spring, the moment curvature response is linear and depends on the spring stiffness parameter K. In the case of the slider element (hereafter referred to as slider), it remains rigid until the applied moment reaches the slip moment threshold B, beyond which slip occurs and the moment becomes constant while the curvature is indeterminate.

In the following, a model capable of predicting the uniaxial bending behavior under constant tensile force of a single-layer strand is first

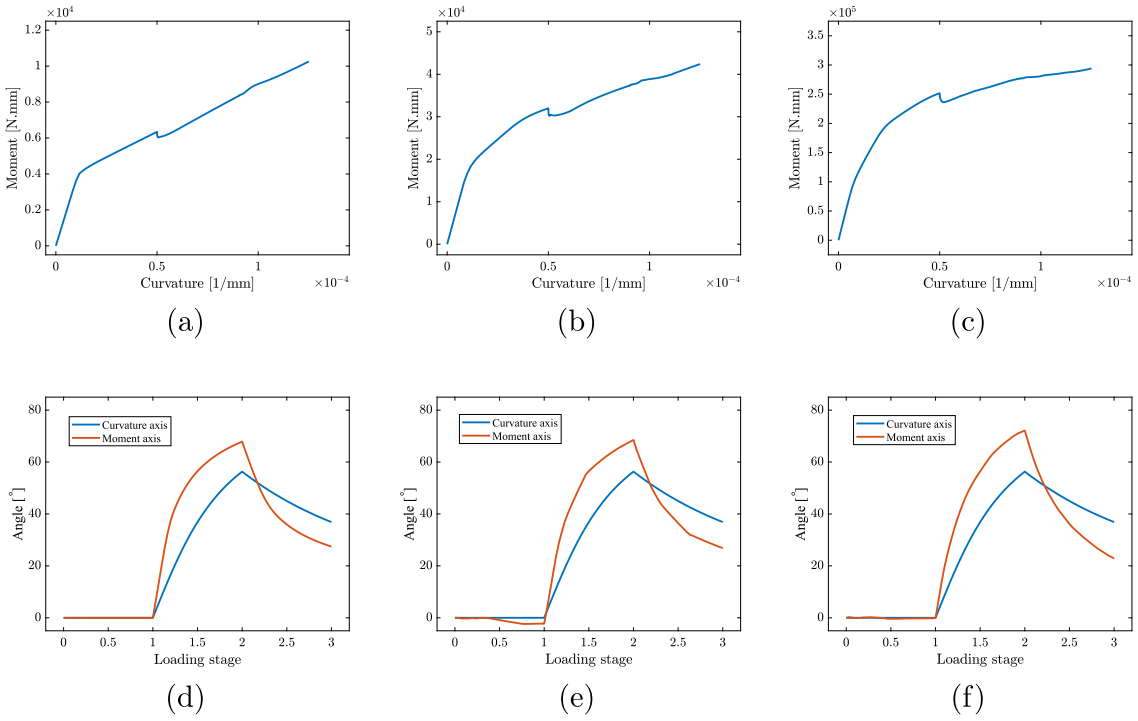

Fig. 10. A comparison of the bending response and the bending axis of spiral strands obtained from homogenization and from the rheological model for the biaxial test case 1. a,d, the single-layer strand; b,e, the two-layer strand; c,f, the four-layer strand.

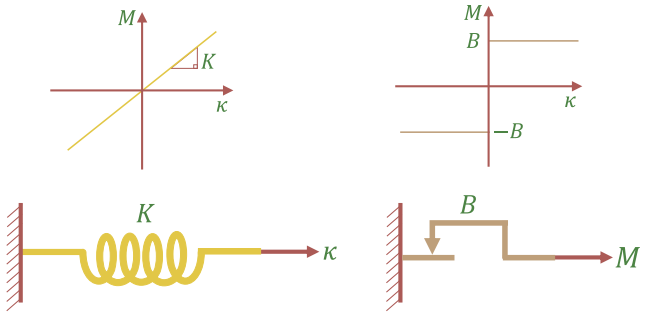

Fig. 11. The rheological elements and their constitutive behavior.

presented, which is then extended to the case of multilayer strands subjected to variable tensile force.

4.1. Uniaxial bending of a single-layer strand under constant tension

The rheological model representing the uniaxial bending response of single-layer strands under constant axial force is first presented as the simplest case. To achieve this, the bending mechanism and various contributions to the bending stiffness, as previously explained, are utilized. As can be seen in Fig. 3, the uniaxial bending response of single-layer strands is bilinear. At low curvatures, the interlayer friction is high enough, and therefore, the first layer provides both the stick and slip contributions to the total bending stiffness of the strand. Therefore, the initial bending stiffness of the strand, K_{initial}, can be calculated as follows:

$$K_{\text{initial}} = K_{\text{slip},0} + K_{\text{slip},1} + K_{\text{stick},1}, \tag{4}$$

where $K_{\text{slip},0}$ represents the slip contribution of the core wire to the bending stiffness, and $K_{\text{slip},1}$ and $K_{\text{stick},1}$ are calculated using (2) and (3), respectively. As the curvature increases, slip occurs between the first layer and the core wire, resulting in the loss of the first layer's sticking contribution to the strands' bending stiffness. At this point, the bending stiffness of the strand can be calculated as:

$$K_{\text{final}} = K_{\text{slip},0} + K_{\text{slip},1}. \tag{5}$$

Since the slip contributions are never lost at any stage of loading, they can be added together and called the slip contribution of the strand, K_{slip}:

$$K_{\text{final}} = K_{\text{slip}} = K_{\text{slip},0} + K_{\text{slip},1}. \tag{6}$$

By removing the subscript 1 from the stick contribution of the first layer from Eq. (4), given that there is only one stick contribution, the bending stiffness contributions can be categorized into two main types, slip and stick contributions. By modeling each of these contributions as a spring, they should be connected in parallel due to their additive nature. However, as mentioned earlier, the stick contribution is lost at some point. To model this loss, a slider element is used in series with the spring representing the stick contribution. The system of spring and slider element acting in series is hereafter referred to as the slider-spring. The rheological model representing a single-layer strand is shown in Fig. 12.

To find the stiffness parameters of the rheological model, the Eqs. (2) and (3) could be used. However, the coefficient β, introduced in Eq. (3) to take the incomplete interlayer load transfer into account, in particular due to the partial contact between the layers, cannot be determined analytically. For this reason, the parameters of the rheological model are identified from the uniaxial bending responses obtained through homogenization. Since in the homogenization approach each contact is explicitly modeled, there is no need for a coefficient like β. This approach ensures that the mechanisms related to the actual contact state between the layers and the dependence on the tensile load, which influence the stick contribution, are accurately accounted for. For this purpose, consider a uniaxial bending response of a single-layer strand under constant tensile force obtained by homogenization, which has been approximated to be bilinear, as shown in Fig. 13. Using this response and Eqs. (4) and (6), the parameters for the rheological model can be obtained as follows:

$$K_{\text{slip}} = \mathcal{K}_2, \tag{7}$$

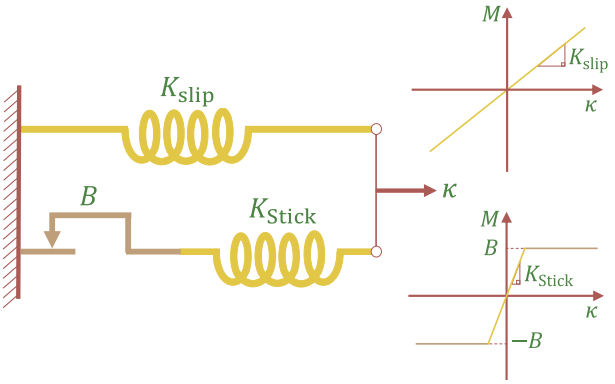

Fig. 12. The rheological model to represent the uniaxial bending behavior of single-layer spiral strands.

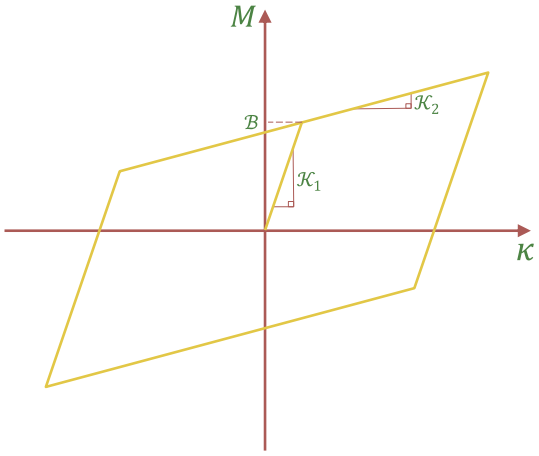

Fig. 13. A bilinear representation of the uniaxial cyclic bending response of a single-layer strand under constant applied tensile force obtained through homogenization.

$$K_{\text{stick}} = \mathcal{K}_1 - \mathcal{K}_2, \tag{8}$$

$$B = \mathcal{B}\left(\frac{\mathcal{K}_1 - \mathcal{K}_2}{\mathcal{K}_1}\right), \tag{9}$$

where B is the slip moment threshold of the first layer, and $\mathcal{K}_1$, $\mathcal{K}_2$ and $\mathcal{B}$ are the successive slopes and the bending moment threshold characterizing the strand response obtained from homogenization, as shown in Fig. 13. Since, due to the parallel connection of the spring and the slider spring, the same curvature is applied to both, the equilibrium of the proposed rheological model is described by the following equation:

$$M = M_{\text{slip}}(\kappa) + M_{\text{stick}}(\kappa), \tag{10}$$

where M, M_{slip}, and M_{stick} are the global bending moment, the moments of the spring and of the slider-spring, respectively. Since the curvature of the spring and the slider-spring are the same in the proposed rheological model, the computational cost can be reduced by using the curvature as the known driving variable and the moment as the unknown. Therefore, with $\square^n$ representing a variable at a given time step n, the moment can be computed as:

$$M^n = M^n_{\text{slip}} + M^n_{\text{stick}}. \tag{11}$$

The moment of the spring is easily calculated by multiplying the applied curvature by the stiffness of the spring as:

$$M^n_{\text{slip}} = K_{\text{slip}}\kappa^n. \tag{12}$$

To calculate the moment of the slider-spring, its equilibrium should be written. Note that since the spring and the slider act in series, the moment is the same in both. To solve the equilibrium of the slider-spring, an elastic predictor-plastic corrector scheme is implemented. In this manner, the moment caused by the applied curvature in the spring is calculated first. If the moment is smaller than the slider's slip moment threshold, no correction is needed and the calculated moment is admissible. However, if the moment is greater than the threshold, it should be corrected and limited to the threshold of the slider. Therefore, the moment of the slider-spring is calculated as follows:

$$M^n_{\text{stick}} = \begin{cases} K_{\text{stick}}\kappa^n, & \text{if } |K_{\text{stick}}\kappa^n| \le B \\ \text{sign}\left(K_{\text{stick}}\kappa^n\right) B, & \text{otherwise} \end{cases} \tag{13}$$

The use of a rheological model to represent the uniaxial response of spiral strands subjected to a constant tensile force has been suggested previously in Cardou (2013). However, in that work, the rheological elements have been connected in series rather than in parallel. The parallel connection proposed here has several advantages. Firstly, each rheological element has a clear physical interpretation, and secondly, for curvature-driven tests, no equilibrium equation needs to be solved in a coupled manner, which is a huge computational advantage. In addition, the use of the homogenized response to extract the rheological parameters has been proposed for the first time in the present study, which makes the prediction of the bending properties more accurate.

4.2. Extension to account for tension variation

The previously described procedure is valid only for a constant tensile force. As shown in Fig. 3, changing the tensile force only scales the strand's behavior without altering its overall shape. Moreover, during the development of the rheological model, no specific assumption was made about the tensile force value. Therefore, varying the tensile force should only affect the model parameters, not the rheological system itself.

To determine the equivalent rheological model for any tensile force, the homogenized uniaxial bending response for that force must be obtained. Since the rheological model remains the same and only the parameters change with tension, the springs stiffnesses and slider element thresholds are considered tension-dependent. These dependencies are approximated by identifying the stiffnesses and slip moment thresholds using several homogenized uniaxial bending responses subjected to different values of constant axial force and using spline interpolation to represent them as continuous functions of the axial force. It should be highlighted that all rheological parameters are found using homogenized moment curvature responses, and no microscopic computations are performed. Once identified, the parameters as functions of the applied tensile force T allow Eq. (10) to be rewritten accordingly.

$$M = M_{\text{slip}}(T, \kappa) + M_{\text{stick}}(T, \kappa). \tag{14}$$

Since the slip contribution to the bending moment does not involve a history parameter, a total formulation is implemented as:

$$M^n_{\text{slip}} = K_{\text{slip}}(T^n)\,\kappa^n, \tag{15}$$

For the stick contribution to the bending moment, as it involves a history parameter determined by the slip moment threshold which is a function of the tensile force, this contribution is expressed incrementally to account for the variation of the tensile force and its effect as follows:

$$M^n_{\text{stick}} = \begin{cases} M^{n-1}_{\text{stick}} + K_{\text{stick}}(T^n)\,\delta\kappa^n, & \text{if } |M^{n-1}_{\text{stick}} + K_{\text{stick}}(T^n)\,\delta\kappa^n| \\ & \le B(T^n) \\ \text{sign}\left(M^{n-1}_{\text{stick}} + K_{\text{stick}}(T^n)\,\delta\kappa^n\right) B(T^n), & \text{otherwise} \end{cases} \tag{16}$$

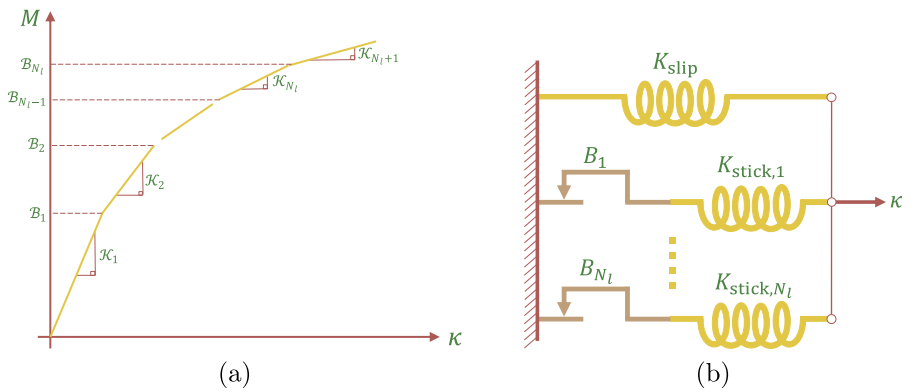

Fig. 14. a, A multilinear representation of the uniaxial cyclic bending response of a N_l-layer strand under constant applied tensile force obtained through homogenization.; b, The rheological model, consisted of a spring and N_l slider-springs, to represent the uniaxial bending behavior of a N_l-layer spiral strand.

where $\delta\kappa^n$ is the increment of the applied curvature. Using Eqs. (15) and (16) to calculate the slip and stick contributions to the bending moment, the effect of variable tensile force in the case of uniaxial bending is considered in the proposed rheological model.

4.3. Extension to consider multilayer strand

To represent the uniaxial bending of a single-layer strand, a rheological model including a spring and a slider-spring acting in parallel has been used. The spring represents the slip contribution of the core wire and the first layer, while the slider-spring represents the stick contribution of the first layer. Based on the explanations provided on the bending mechanism of the spiral strands, to extend the framework of the rheological model to represent a N_l-layer spiral strand, a spring acting in parallel with N_l slider-springs should be used (Fig. 14). The spring represents the slip contribution of all strand wires, while each slider-spring represents the stick contribution of a layer. In addition, the effect of a variable tensile force is taken into account by considering the parameters of the spring and slider elements as tension-dependent.

To find the parameters for the rheological model, the uniaxial responses obtained from homogenization are approximated to be multilinear, as shown in Fig. 14. The initial bending stiffness observed in the global moment curvature response, is the sum of all the slip and stick contributions to the bending stiffness of all layers, as follows:

$$\mathcal{K}_1 = K_{\text{slip}} + \sum_{l=1}^{N_l} K_{\text{stick},l}. \tag{17}$$

As the curvature increases, first the stick contribution of the N_l^{th} layer is lost, and this loss then propagates towards the inner layers until all stick contributions to the bending stiffness are zero. For any bending stiffness observed in the global moment curvature response of the strand, $\mathcal{K}_m$, the following expression can be written:

$$\mathcal{K}_m = K_{\text{slip}} + \sum_{l=1}^{N_l-m+1} K_{\text{stick},l}, \qquad m = 1, \dots, N_l + 1. \tag{18}$$

From the above equation, the slip and stick contributions to the bending stiffness for all layers can be calculated.

To find the slip moment thresholds, the bending moment between two successive thresholds $\mathcal{B}_m$ and $\mathcal{B}_{m+1}$ is considered. Between these two thresholds, layers from N_l-m+1 to N_l have lost their stick contribution to the bending stiffness, and consequently their contribution to the bending moment is constant and equal to their slip moment thresholds. The expression for the bending moment in this case is:

$$\begin{aligned} M &= \sum_{l=N_l-m+1}^{N_l} B_l + \left(K_{\text{slip}} + \sum_{l=1}^{N_l-m} K_{\text{stick},l} \right) \kappa \\ &= \sum_{l=N_l-m+1}^{N_l} B_l + \mathcal{K}_{m+1}\kappa. \end{aligned} \tag{19}$$

The layer $N_l - m$ slips at the curvature κ_{m+1} such that:

$$B_{N_l-m} = K_{\text{stick},N_l-m}\kappa_{m+1}. \tag{20}$$

This curvature can be calculated from (19) as:

$$\kappa_{m+1} = \frac{\mathcal{B}_{m+1} - \sum_{l=N_l-m+1}^{N_l} B_l}{\mathcal{K}_{m+1}}. \tag{21}$$

Inserting (21) into (20), the slip moment threshold for any layer $N_l - m$ is calculated as:

$$B_{N_l-m} = \frac{K_{\text{stick},N_l-m}}{\mathcal{K}_{m+1}} \left(\mathcal{B}_{m+1} - \sum_{l=N_l-m+1}^{N_l} B_l \right). \tag{22}$$

Having all the parameters for the rheological elements, the final equation to be solved for the rheological model is:

$$M = M_{\text{slip}}(T, \kappa) + \sum_{l=1}^{N_l} M_{\text{stick},l}(T, \kappa), \tag{23}$$

which is solved incrementally using (15) for the spring and (16) for each slider-spring, individually.

5. The multiaxial rheological model

Thus far, the uniaxial bending behavior of spiral strands subjected to variable tensile force has been described. The next goal is to describe the biaxial bending behavior of spiral strands. For this purpose, an approach inspired by the concept of microsphere, which is widely used in the micromechanical modeling of hyperelastic materials (see, for example, Miehe et al., 2004), is employed.

As long as only uniaxial bending is considered, that is, bending is always about the same axis, curvature and moment are implicitly defined with respect to this fixed axis. In the following, the rheological model for uniaxial bending introduced in the previous section, which can be associated with any fixed bending axis, will be referred to as a uniaxial spring system. However, when dealing with bending about varying axes, the orientation of these axes must be explicitly considered. The aim of this section is to propose a more general rheological model capable of modeling the bending response of a strand when the bending axis orientation changes with the loading.

When considering bending about an axis, a single history variable is sufficient to track the slip/stick state for an interlayer. However, as illustrated in Fig. 9, this single history variable reflects a complex slip pattern in different directions. By applying increments of curvatures about varying bending axis, the slipping status for each interlayer in each direction will be affected differently depending not only on the relative orientation with respect to the current bending axis, but also on the previous status in this direction, as illustrated by the typical anisotropic behavior depicted in Fig. 8. This observation suggests that

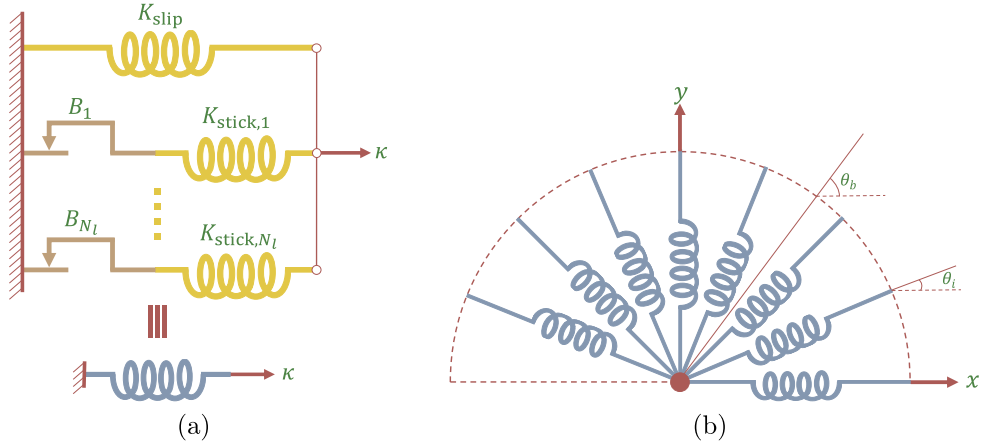

Fig. 15. a, The equivalent rheological models consisted of a uniaxial spring system to represent the uniaxial response of spiral strands; b, The rheological model consisted of a multiaxial spring system to represent the biaxial bending behavior of spiral strands.

a history variable for each interlayer should be associated with each orientation.

The objective of the proposed model is to discretize the possible orientations of the bending axis by assigning a uniaxial spring system to each discrete orientation. In this way, a history variable is assigned to each interlayer and to each discrete orientation angle. The proposed model capable of representing the bending response in all directions simultaneously is thus formulated as a multiaxial spring system consisting of n_θ equally spaced uniaxial spring systems, as shown in Fig. 15, with $\tilde{K}_{slip}$, $\tilde{K}_{stick}$ and $\tilde{B}$ as parameters for the rheological elements. Since individual uniaxial spring systems behave symmetrically with respect to the sign of the curvature, they can be distributed over only half a circle, and therefore $0 \leq \theta_i < 180°$.

As illustrated in Fig. 9, when an increment of curvature in a given direction is applied to a strand, it affects the history variable in all directions. Therefore, a key question in formulating the multiaxial spring system is how an applied increment of curvature influences the history variable in various directions. To address this, we adopt the assumption used in Papailiou (1995) and Foti and Martinelli (2016b). In these works, the increment of additional interlayer friction stress, which drives interlayer slip and consequently the history variable, is assumed to follow a sinusoidal distribution across the cross-section. Drawing inspiration from these studies, we assume that the increment of curvature, which drives the history variable in our model, also exhibits a sinusoidal distribution in the multiaxial spring system. Therefore, to determine the increment of curvature acting on each uniaxial spring system, we project the applied increment of curvature onto the direction of the uniaxial spring system. It is further assumed that the moment of each uniaxial spring system is expressed as a vector collinear with the unit directional vector of that system. The resultant moment of the multiaxial system is then expressed as the sum of the individual vector contributions from all uniaxial spring systems.

To formulate the multiaxial system, all vectorial quantities are expressed in the global coordinate system, taking into account the orientation θ_i of each uniaxial spring system, and the orientation θ_b of the current bending axis (see Fig. 15).

The curvature increment $\delta\kappa_b$ can be decomposed into its two components in the global coordinate system, $\delta\kappa_x$ and $\delta\kappa_y$, as follows:

$$\begin{bmatrix}\delta\kappa_x\\ \delta\kappa_y\end{bmatrix} = \begin{bmatrix}\cos(\theta_b)\\ \sin(\theta_b)\end{bmatrix}\delta\kappa_b. \tag{24}$$

The increment of curvature acting on each uniaxial spring system, $\delta\kappa_i$, can be calculated as follows:

$$\delta\kappa_i = \begin{bmatrix}\cos(\theta_i) & \sin(\theta_i)\end{bmatrix}\begin{bmatrix}\delta\kappa_x\\ \delta\kappa_y\end{bmatrix} = \begin{bmatrix}\cos(\theta_i) & \sin(\theta_i)\end{bmatrix}\begin{bmatrix}\cos(\theta_b)\\ \sin(\theta_b)\end{bmatrix}\delta\kappa_b = \cos(\theta_b-\theta_i)\,\delta\kappa_b. \tag{25}$$

Given the number of discretizations in the angular direction and the curvature increment (either $\delta\kappa_x$ and $\delta\kappa_y$, or $\delta\kappa_b$), one can compute the curvature increment of any uniaxial spring system, and thus its moment, $\tilde{M}_i$, from (23). Note that using $\tilde{\square}$ indicates the use of multiaxial spring system parameters. Once the moment contribution of all uniaxial spring systems is known, the resulting moment is calculated as the sum of contributions of all uniaxial spring systems as:

$$\begin{bmatrix}\tilde{M}_x\\ \tilde{M}_y\end{bmatrix} = \sum_{i=1}^{n_\theta}\begin{bmatrix}\cos(\theta_i)\\ \sin(\theta_i)\end{bmatrix}\tilde{M}_i, \tag{26}$$

where $\tilde{M}_x$ and $\tilde{M}_y$ are the bending moments in the x- and y-directions of the multiaxial spring system, respectively.

To find the parameters of the rheological elements for the multiaxial spring system, the uniaxial responses of the multiaxial system and a uniaxial spring system are required to be equal in two extreme cases. The stiffnesses, $\tilde{K}_{slip}$ and $\tilde{K}_{stick}$, are obtained by considering the case where no slip has occurred in any of the uniaxial spring systems, and the slip moment thresholds, $\tilde{B}$, are obtained by assuming that slip has occurred in all of the uniaxial spring systems.

Considering the no-slip assumption and monotonic loading, and using (12) and (13), the response of the uniaxial spring system can be calculated as:

$$M = \left(K_{slip} + \sum_{l=1}^{N_l} K_{stick,l}\right)\kappa, \tag{27}$$

For the multiaxial spring system, it would be more convenient for comparison purposes to compute the moment in the θ_b direction. By noting $\tilde{M}_{b,1}$ and $\tilde{M}_{b,2}$ as the moment in the θ_b and its normal direction, respectively, we have:

$$\begin{aligned}\begin{bmatrix}\tilde{M}_{b,1}\\ \tilde{M}_{b,2}\end{bmatrix} &= \sum_{i=1}^{n_\theta}\begin{bmatrix}\cos(\theta_b-\theta_i)\\ \sin(\theta_b-\theta_i)\end{bmatrix}\left(\left(\tilde{K}_{slip}+\sum_{l=1}^{N_l}\tilde{K}_{stick,l}\right)\cos(\theta_b-\theta_i)\,\kappa_b\right)\\ &= \sum_{i=1}^{n_\theta}\begin{bmatrix}\cos^2(\theta_b-\theta_i)\\ \cos(\theta_b-\theta_i)\sin(\theta_b-\theta_i)\end{bmatrix}\left(\tilde{K}_{slip}+\sum_{l=1}^{N_l}\tilde{K}_{stick,l}\right)\kappa_b\\ &= \begin{bmatrix}\frac{n_\theta}{2}\\ 0\end{bmatrix}\left(\tilde{K}_{slip}+\sum_{l=1}^{N_l}\tilde{K}_{stick,l}\right)\kappa_b.\end{aligned} \tag{28}$$

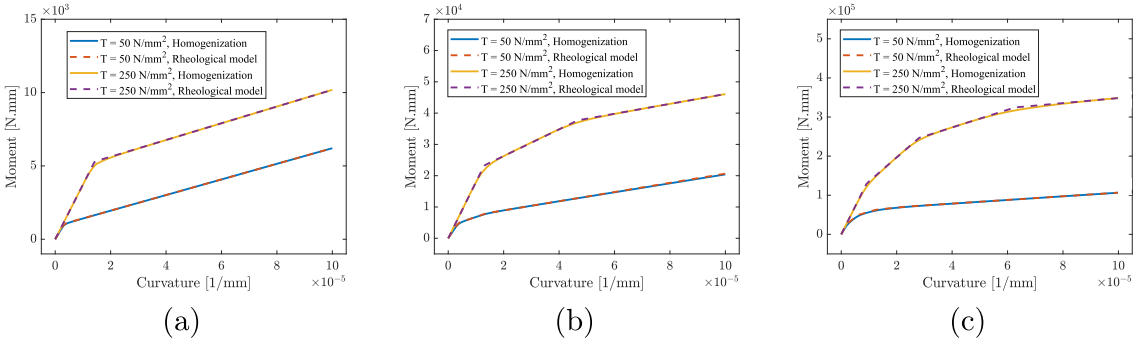

Fig. 16. A comparison of the bending response of spiral strands obtained from homogenization and from the rheological model using only a uniaxial spring system, for the uniaxial test case 1. a, the single-layer strand; b, the two-layer strand; c, the four-layer strand.

where considering $n_\theta > 3$, the following identities, demonstrated using Mathematica (Inc., 2023), have been used:

$$\begin{aligned}
&\sum_{i=1}^{n_\theta} \cos^2\left(\theta_b - \theta_i\right) = \sum_{i=1}^{n_\theta} \cos^2\left(\theta_b - (i-1)\,\frac{\pi}{n_\theta}\right) = \frac{n_\theta}{2},\\
&\sum_{i=1}^{n_\theta} \cos\left(\theta_b - \theta_i\right)\sin\left(\theta_b - \theta_i\right) = \sum_{i=1}^{n_\theta} \cos\left(\theta_b - (i-1)\,\frac{\pi}{n_\theta}\right)\\
&\qquad\qquad \times \sin\left(\theta_b - (i-1)\,\frac{\pi}{n_\theta}\right) = 0.
\end{aligned} \tag{29}$$

Due to the no-slip assumption, the behavior of the strand is linear elastic and $\tilde{M}_{b,2} = 0$. By comparing the uniaxial moment of Eq. (27) with $\tilde{M}_{b,1}$ of Eq. (28), and setting them to be equal, the stiffnesses of the multiaxial system should be scaled as follows:

$$\begin{aligned}
\tilde{K}_{\text{slip}} &= \frac{2K_{\text{slip}}}{n_\theta},\\
\tilde{K}_{\text{stick},l} &= \frac{2K_{\text{stick},l}}{n_\theta},
\end{aligned} \tag{30}$$

where K_{slip} and $K_{\text{stick},l}$ are the stiffnesses obtained from Eq. (18).

The modified sliding thresholds are obtained by assuming that slip has occurred in all uniaxial spring systems. By considering monotonic loading in the θ_b direction, that is $\kappa_b > 0$, and by ignoring the slip contribution to the bending moment of all uniaxial spring systems, using (13), the moment of the multiaxial system is calculated as:

$$\begin{aligned}
\begin{bmatrix}\tilde{M}_{b,1}\\ \tilde{M}_{b,2}\end{bmatrix} &= \sum_{i=1}^{n_\theta}\begin{bmatrix}\cos\left(\theta_b - \theta_i\right)\\ \sin\left(\theta_b - \theta_i\right)\end{bmatrix}\tilde{M}_i = \sum_{i=1}^{n_\theta}\begin{bmatrix}\cos\left(\theta_b - \theta_i\right)\\ \sin\left(\theta_b - \theta_i\right)\end{bmatrix}\sum_{l=1}^{N_l}\text{sign}\left(\kappa_i\right)\tilde{B}_l\\
&= \sum_{i=1}^{n_\theta}\begin{bmatrix}\cos\left(\theta_b - \theta_i\right)\\ \sin\left(\theta_b - \theta_i\right)\end{bmatrix}\sum_{l=1}^{N_l}\text{sign}\left(\cos\left(\theta_b - \theta_i\right)\kappa_b\right)\tilde{B}_l\\
&= \sum_{i=1}^{n_\theta}\begin{bmatrix}\cos\left(\theta_b - \theta_i\right)\text{sign}\left(\cos\left(\theta_b - \theta_i\right)\right)\\ \sin\left(\theta_b - \theta_i\right)\text{sign}\left(\cos\left(\theta_b - \theta_i\right)\right)\end{bmatrix}\sum_{l=1}^{N_l}\tilde{B}_l\\
&= \sum_{i=1}^{n_\theta}\begin{bmatrix}\left|\cos\left(\theta_b - \theta_i\right)\right|\\ 0\end{bmatrix}\sum_{l=1}^{N_l}\tilde{B}_l.
\end{aligned} \tag{31}$$

In this case, the response of a uniaxial spring system is simply calculated as:

$$M = \sum_{l=1}^{N_l} B_l, \tag{32}$$

By comparing Eqs. (31) and (32), the sliding threshold should be scaled by the factor $1/\sum_{i=1}^{n_\theta}\left|\cos\left(\theta_b - \theta_i\right)\right|$. It can be observed that, unlike the modification parameter for the stiffness parameter, this modification depends on the direction of the applied curvature. However, if the number of discretizations is more than 20, the variation caused by the choice of θ_b is less than one percent. Therefore, assuming that more than 20 uniaxial springs are used in the multiaxial spring system, the sliding thresholds can be modified as follows:

$$\tilde{B} = \frac{B}{\sum_{i=1}^{n_\theta}\left|\cos\left(\theta_i\right)\right|}. \tag{33}$$

Table 2
Parameters for the uniaxial rheological model representing the single-layer strand.

Tension [N/mm²]	K_{slip} [N mm²]	K_{stick} [N mm²]	B [N mm]
0	52 215 318	280 543 407	0
100	54 191 783	292 874 980	1769
200	56 072 335	310 758 817	3568
300	57 921 050	317 538 126	5411

6. Numerical examples

The previous section discussed the framework of the rheological model capable of describing the biaxial bending response of spiral strands subjected to variable tensile force. In this section, the robustness and accuracy of the proposed model is illustrated through some numerical examples. The three spiral strands with geometric properties of Table 1 are considered again (Fig. 2), and are used for all numerical examples in this section. After finding the required parameters for setting up the rheological model, six uniaxial and three biaxial loading histories are defined. To explore the capabilities of the proposed scheme, the results obtained from the proposed rheological model are compared with the homogenized responses obtained from solving an RVE BVP. Since the results of the computational homogenization for spiral strands have already been verified against DNS in Saadat and Durville (2023), no verification against DNS is presented here.

6.1. Parameter identification

As mentioned earlier, the results of several monotonic uniaxial bending tests under constant tensile force are required to obtain the parameters for different springs of the rheological model. Therefore, the four bending responses shown in Fig. 3 are used to obtain the parameters of the rheological model representing the strands. The parameters of the uniaxial rheological model for the single-layer strand are presented in Table 2. The parameters for the multiaxial rheological model can be obtained from Eqs. (30) and (33), once the number of angular discretizations has been determined. The variations of the parameters as a function of the tensile stress are approximated using a cubic spline interpolation.

6.2. Uniaxial bending

6.2.1. Uniaxial bending test case 1

A uniaxial bending test under a constant tensile force that has not been used in the parameter identification procedure is the most

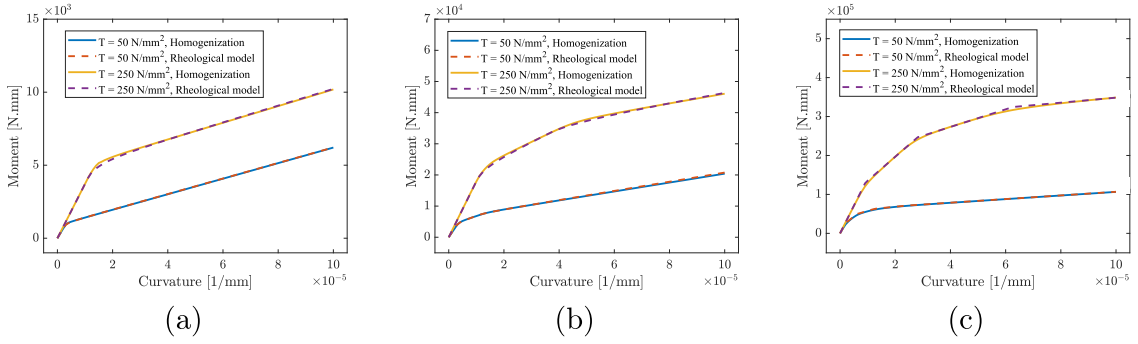

Fig. 17. A comparison of the bending response of spiral strands obtained from homogenization and from the rheological model using the multiaxial spring system, for the uniaxial test case 1. a, the single-layer strand; b, the two-layer strand; c, the four-layer strand.

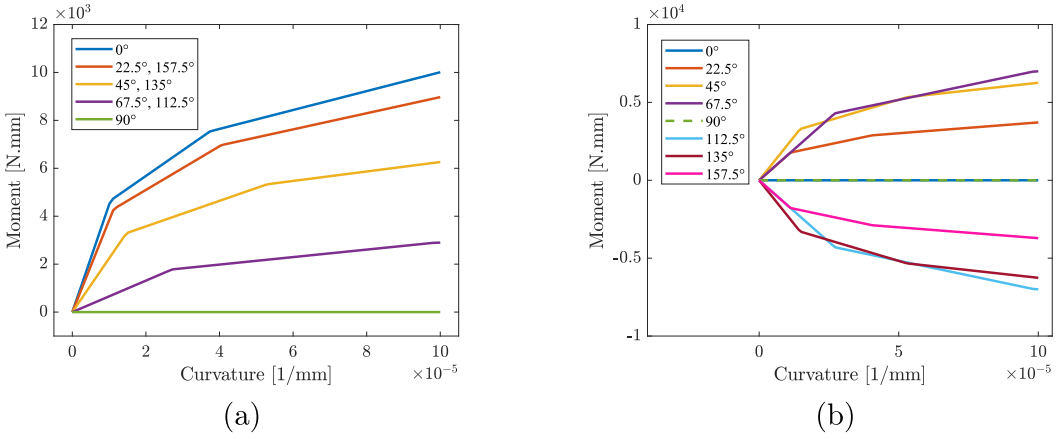

Fig. 18. The moment distribution over the 8 discrete uniaxial spring systems in the multiaxial spring system of a two-layer strand subjected to uniaxial bending. a, x-axis; b, y-axis.

straightforward loading history that could be defined to assess the validity of the proposed scheme. This simple case, which assesses the validity of interpolation of the spring parameters as a function of the tensile force, will be covered in two manners. First, after identifying the model parameters for different strands (the parameters of the single-layer strand are given in Table 2), only a uniaxial spring system is considered; therefore, the spring parameters need no modification. Second, a multiaxial spring system is considered, and modifications are required for the spring parameters, as defined in Eqs. (30) and (33).

As tensile stresses of 0, 100, 200, and 300 N/mm^2 have been used to find the spring parameters, tensile stresses of 50 and 250 N/mm^2 are considered for this example. The results using only a uniaxial spring system are presented in Fig. 16 for all strands and are compared against the results obtained from homogenization. As it can be observed, the results are in good agreement with the homogenized responses.

For the multiaxial spring system, the modified spring parameters are calculated from Eqs. (30) and (33), considering 20 uniaxial spring systems are used. The responses of strands considering these assumptions are depicted in Fig. 17.

To understand the behavior of the multiaxial spring system, the behavior of different uniaxial spring systems in different directions is analyzed for the multiaxial system representing the two-layer strand. However, for the sake of illustration, let us consider 8 uniaxial spring systems instead of 20 for the multiaxial spring system. Fig. 18 shows the moment of each of the 8 uniaxial spring systems in x- and y-axes. It can be observed that a uniaxial curvature in the x-axis has caused a moment in all systems (except the one perfectly perpendicular to the loading direction) in both x- and y-axes. Interestingly, although the behavior of each uniaxial spring system is multilinear, the resultant moment in the x-axis, plotted in Fig. 17 has a smooth transition at the onset of

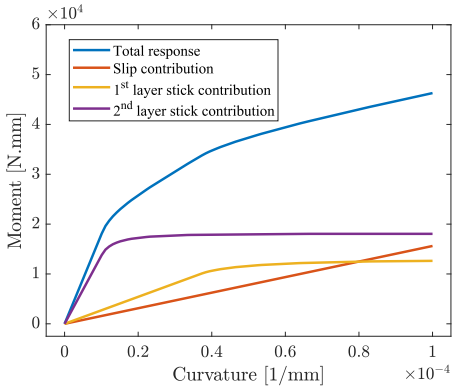

Fig. 19. Different contributions to the bending response of the two-layer spiral strand subjected to uniaxial test case 1, based on the rheological model.

slip of each layer, since slip occurs at different curvatures in different directions. This smooth transition, due to the slight offset between the triggering of slip for the uniaxial spring systems in different directions, is similar to the transition observed in the homogenization results.

To further explore the behavior of the proposed rheological model, the different contributions to the total bending moment response of the strand are shown in Fig. 19. Three different contributions, namely the slip contribution of all wires, and the stick contribution of the first and second layers, constitute the response of a two-layer spiral strand. It can be seen that at low curvatures no interlayer slip has occurred between the layers and all three contributions are present. As the curvature increases, the stick contribution of the second layer is lost, followed by

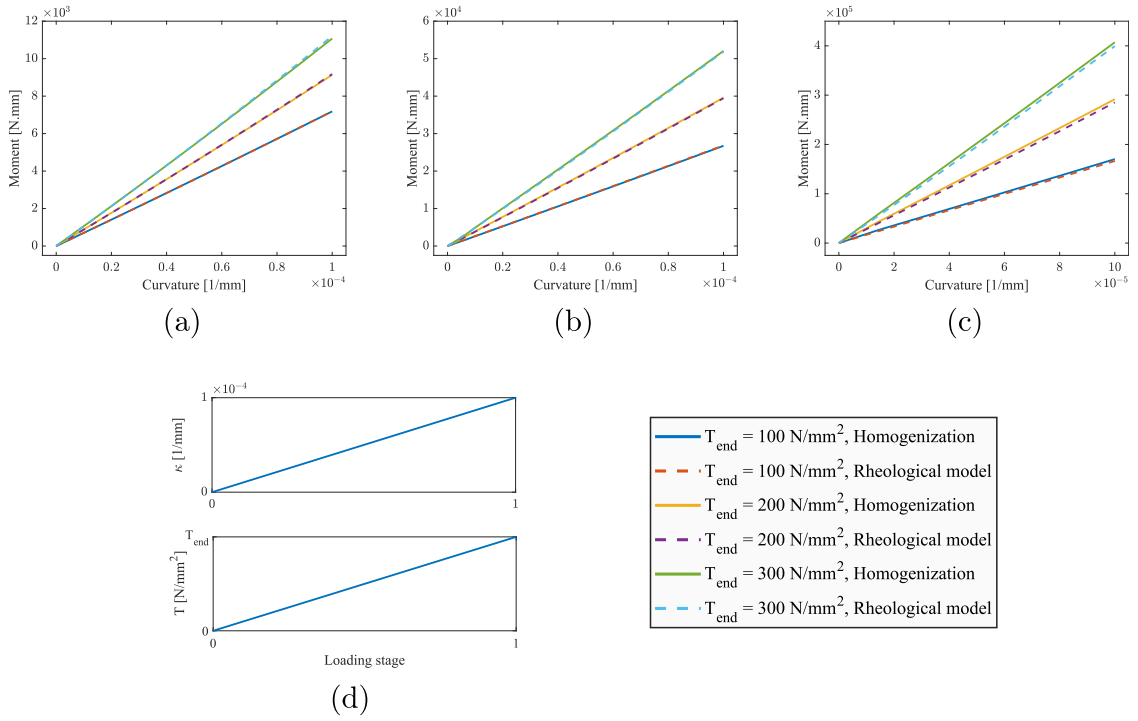

Fig. 20. A comparison of the bending response of spiral strands obtained from homogenization and from the rheological model for the uniaxial test case 2. a, the single-layer strand; b, the two-layer strand; c, the four-layer strand; d, the loading history.

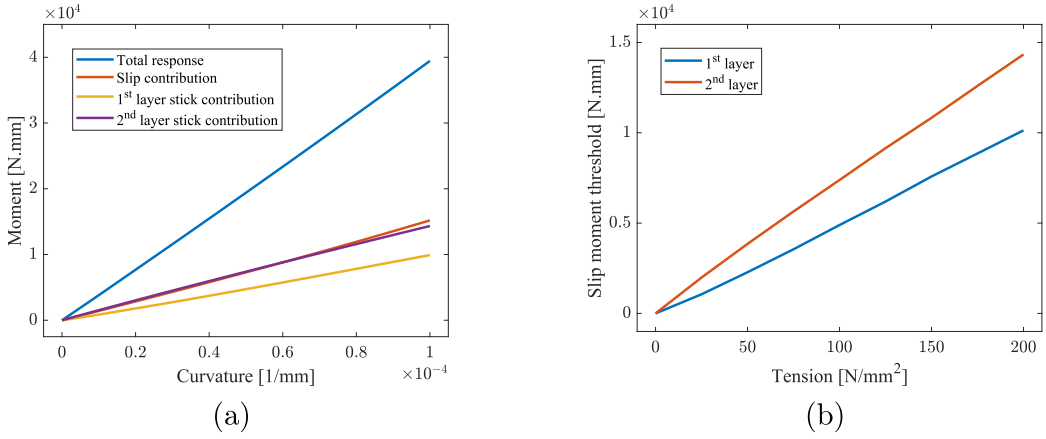

Fig. 21. The two-layer spiral strand subjected to the uniaxial bending test case 2 with T_{end} = 200 N/mm^2. a, The different contributions to the bending moment; b, The slip moment thresholds of the different layers.

that of the first layer, until only the slip contribution of all the wires remains, which is the expected behavior of a two-layer spiral strand subjected to a constant tensile force.

6.2.2. *Uniaxial bending test case 2*

As the second uniaxial load case, the validity of the proposed rheological model in capturing the effect of the variation of the axial force is investigated. In this load case, which has already been explained in 3.2 using computational homogenization, the bending curvature and the axial force are increased proportionally. A comparison of the results obtained from the homogenization and the rheological models is depicted in Fig. 20, which shows a good level of agreement.

To investigate the validity of the proposed explanation for the observed linear behavior of the strands in this load case, consider the two-layer spiral strand and the case with T_{end} = 200 N/mm^2. The different contributions to the bending moment along with the slip moment thresholds of the two layers are illustrated in Fig. 21. It can be observed that the stick contributions of the first and second layers to the bending moment in this case are equal to their slip moment thresholds, each of which varies linearly with respect to the applied axial force. This demonstrates the capabilities of the proposed rheological model not only to predict the bending response of spiral strands, but also to provide some insight into why they exhibit such a response.

6.2.3. *Uniaxial bending test case 3*

In this load case, already treated in 3.2, the axial force decreases proportionally as the bending curvature increases. A comparison of the results obtained from the homogenization and the rheological models is illustrated in Fig. 22, which shows a good level of agreement.

The different contributions to the bending moment of the two-layer spiral strands for the case with T_0 = 200 N/mm^2 are shown in Fig. 23. It can be observed that initially, when no interlayer slip has occurred, the stick contribution of both layers to the bending moment is increasing. However, once slip occurs, the moment contribution

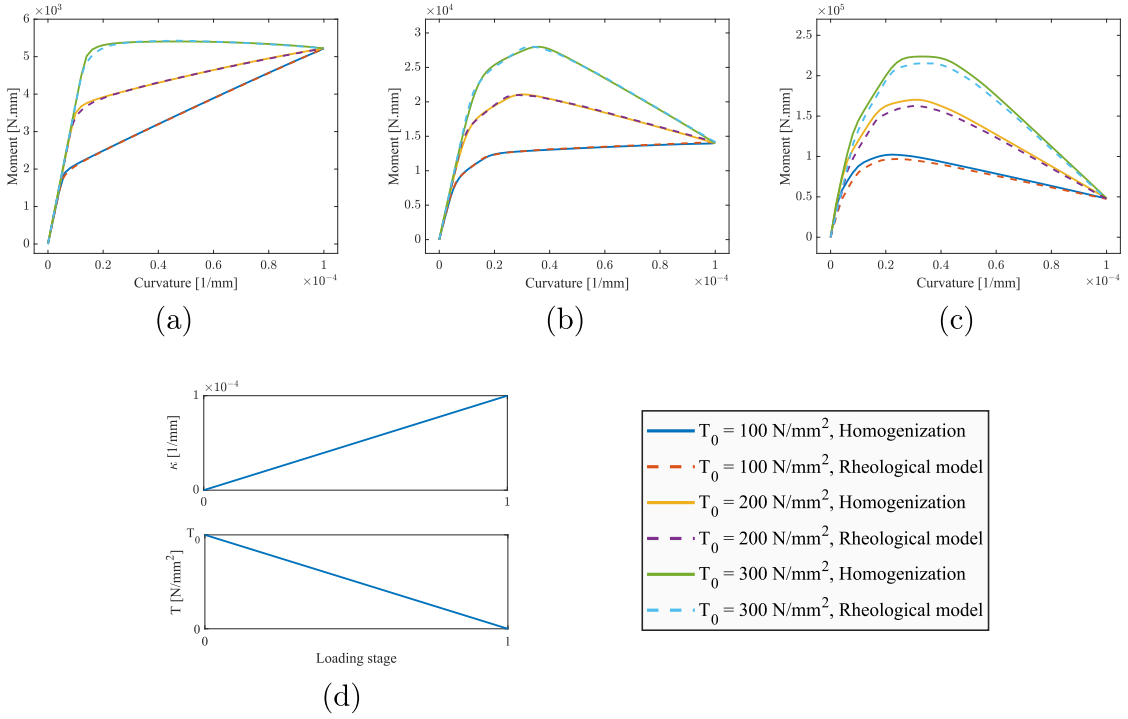

Fig. 22. A comparison of the bending response of spiral strands obtained from homogenization and from the rheological model for the uniaxial test case 3. a, the single-layer strand; b, the two-layer strand; c, the four-layer strand; d, the loading history.

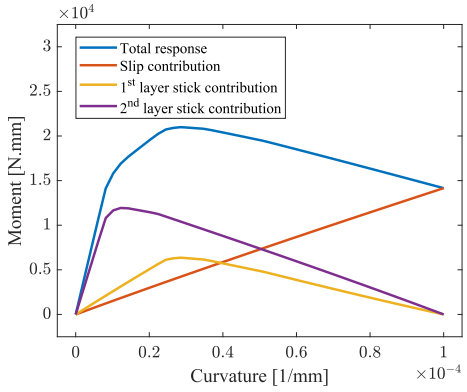

Fig. 23. Different contributions to the bending response of the two-layer spiral strand subjected to the uniaxial test case 3 with $T_0 = 200$ N/mm^2, based on the rheological model.

decreases instead of remaining constant. The reason for this is that in this load case, the tension decreases, causing the slip moment threshold, which determines the post-slip moment contribution of the layer, to decrease. Therefore, in accordance with the explanation given in the previous section, there are two competing mechanisms in the strand, the slip contribution, which is increasing, and the stick contributions, which are decreasing, as can be observed. In this case, since the slope of the decrease of the slip moment thresholds of the two layers is greater than the slip contribution, the overall response is decreasing and a softening behavior is observed.

6.2.4. Uniaxial bending test case 4

The last uniaxial bending test case considers a very complex loading history. In this loading case, the cyclic response of the strands is evaluated under extreme changes in the applied tensile force. A comparison of the rheological model responses with the homogenized responses is shown in Fig. 24. It can be observed that the results of the proposed rheological model are in good agreement with the homogenized responses, and the proposed models have captured the complex bending behavior of spiral strands.

6.3. Biaxial bending

Since the reason for using a multiaxial spring system is to capture the biaxial response of spiral strands, the capabilities of the proposed model in reproducing the biaxial response are illustrated through some test cases in this section. For each numerical example, the results using the x and y components of the applied curvature and bending moment vectors are shown first, followed by the results using the amplitude of the vectors and their angle with respect to the x-axis.

6.3.1. Biaxial bending test case 1

The first biaxial test case, previously explored in 3.3, consists of three successive different loading stages under the assumption of a constant tensile force. After a uniaxial bending about the x-axis, the curvature in this direction is kept constant and a uniaxial bending about the y-axis is performed. In the last stage, the curvature in y-axis is kept constant and the curvature in x-axis is further increased. This load history and the responses of the strands are shown in Fig. 25.

The key aspect of this test case is the bending-induced anisotropy. Spiral strands, in their intact form, are radially symmetric, leading to uniform bending stiffness in all directions. However, loading along the x-axis alters the bending stiffness in the y-axis, as the stiffness in the y-axis is lower than in the x-axis. To capture this induced anisotropy, it is crucial to track different history variables in different directions. Fig. 18 illustrates that uniaxial bending results in varied moments and history variables across directions, demonstrating how the proposed multiaxial spring system can capture this anisotropy, as shown in Fig. 25.

A noticeable drop in bending moment about the x-axis occurs during the second loading stage. Eight uniaxial spring systems are used to model the single-layer strand and explain this drop. In the first stage, as detailed previously, curvatures of all systems increase in absolute value, even if some are negative, as seen in Fig. 26. In the second stage,

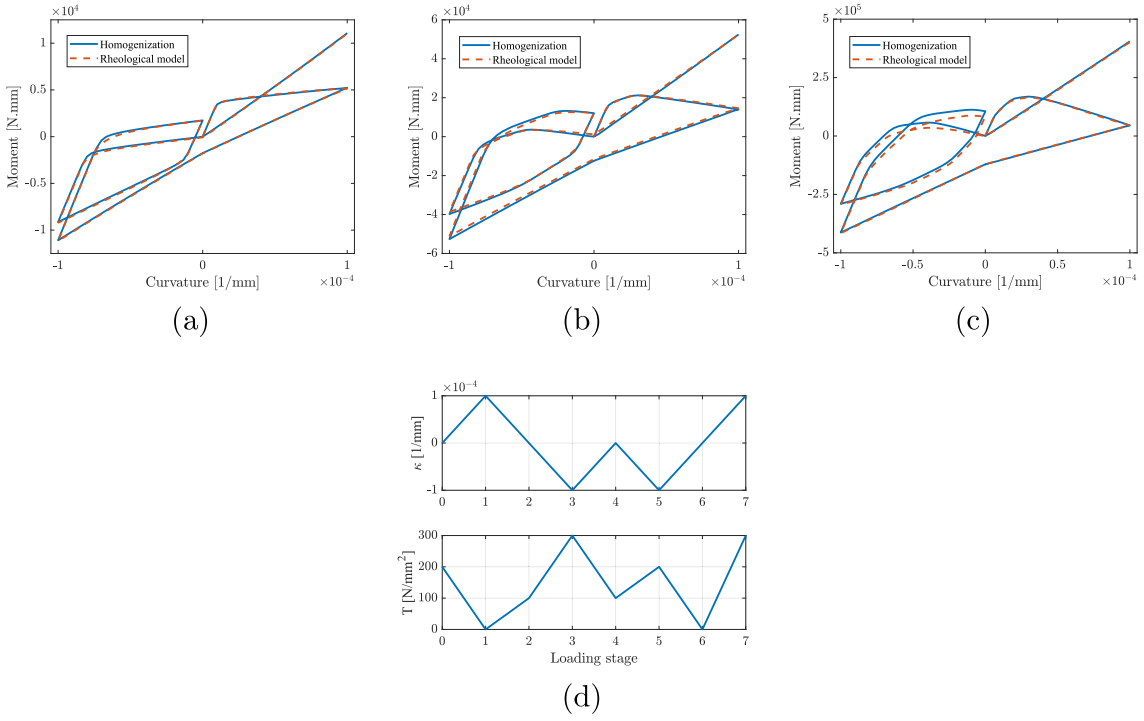

Fig. 24. A comparison of the bending response of spiral strands obtained from homogenization and from the rheological model for the uniaxial test case 4. a, the single-layer strand; b, the two-layer strand; c, the four-layer strand; d, the loading history.

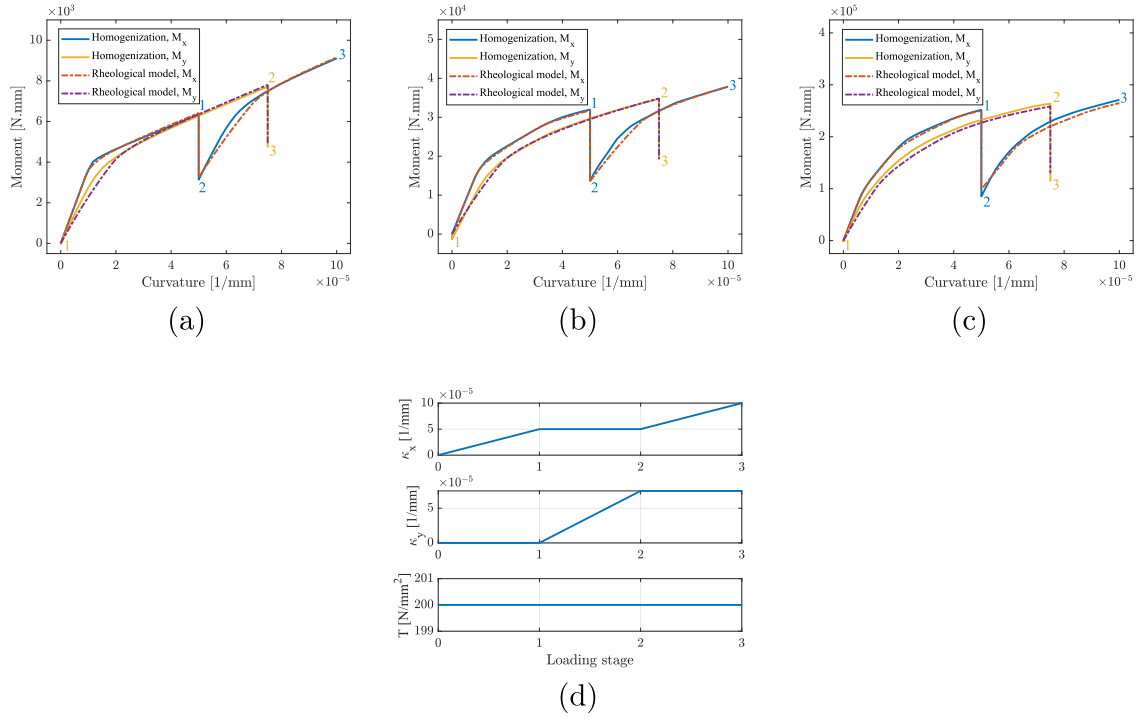

Fig. 25. A comparison of the bending responses in the x- and y-axes of spiral strands obtained from homogenization and from the rheological model for the biaxial test case 1 (the end of each load stage is marked on each curve). a, the single-layer strand; b, the two-layer strand; c, the four-layer strand; d, the loading history.

a change in bending axis direction causes some systems to unload and then reload in the opposite direction, leading to the observed drop in the response about the x-axis. Moments about the x- and y-axes, shown in Fig. 26, highlight this loading–unloading behavior. In the final stage, a similar drop is observed, but this time about the y-axis.

A comparison of the results using the amplitude of the bending moment vector and its angle with respect to the x-axis is illustrated in Fig. 27, which shows good agreement between the results obtained from homogenization and the rheological model.

6.3.2. *Biaxial bending test case 2*

As the second biaxial test case, a very complex cyclic loading history is considered under variable tensile force, including simultaneous loading about the x- and y-axes. The loading history and the responses of

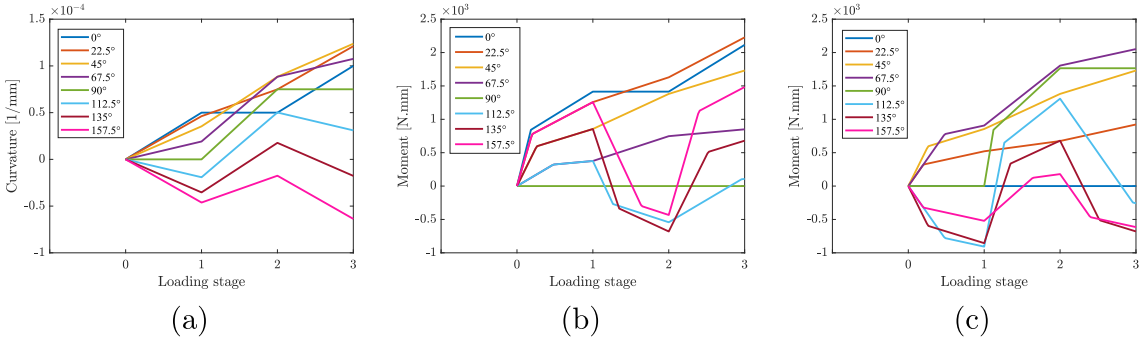

Fig. 26. Distribution of moment and curvature in the multiaxial spring system representing the single layer strand, subjected to the biaxial test case 1 loading. a, curvature; b, moment about the x-axis; c, moment about the y-axis.

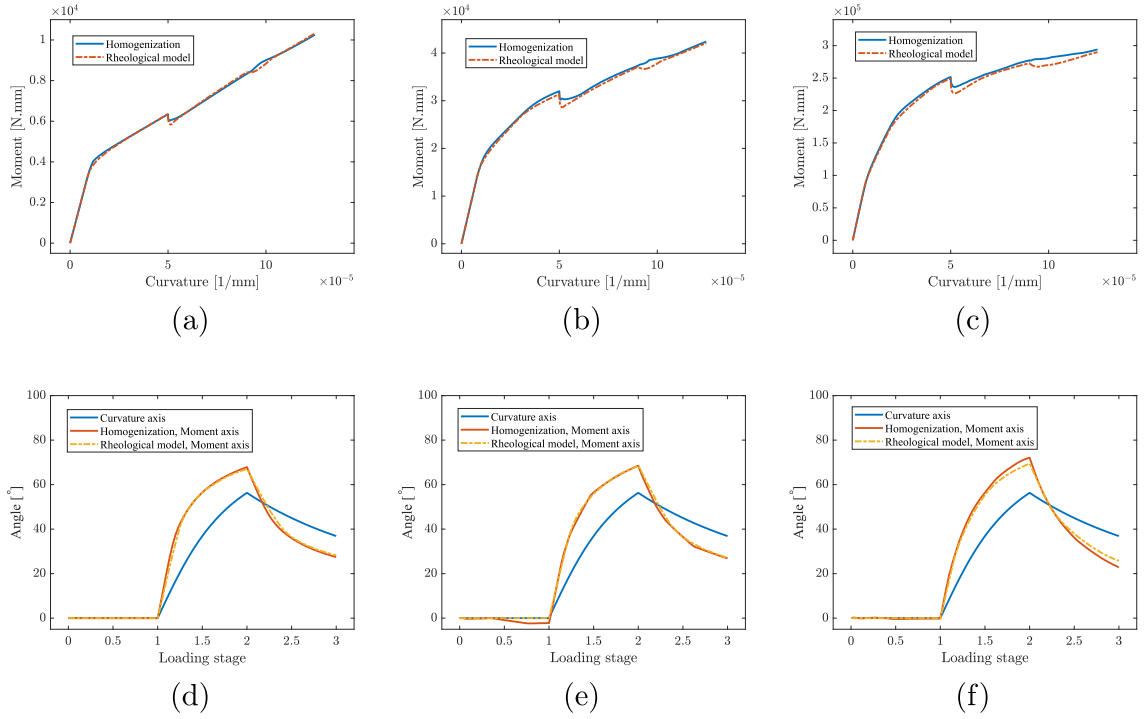

Fig. 27. A comparison of the bending response and the bending moment axis of spiral strands obtained from homogenization and from the rheological model for the biaxial test case 1. a,d, the single-layer strand; b,e, the two-layer strand; c,f, the four-layer strand.

the strands are shown in Figs. 28 and 29. A good agreement is observed when comparing the results of the proposed rheological model with the homogenized responses, which indicates the robustness and accuracy of the proposed model.

7. Conclusions

A rheological constitutive model equivalent to multilayer spiral strands, capable of predicting their anisotropic biaxial bending behavior under variable tensile force, has been presented in this paper. For this purpose, for the first time, the effect of variation of axial force and bending axis on the bending behavior of these strands has been investigated using the mixed stress–strain driven computational homogenization. It has been shown that the uniaxial bending response of spiral strands is strongly influenced by the variation of the axial force, and the nearly multilinear response expected from these strands when they are subjected to a constant axial force can take many different forms, e.g., nearly linear, or they can even exhibit softening behavior. Furthermore, by studying the biaxial behavior of these strands, an induced anisotropy has been observed, due to different onset of interlayer slip in different orientations. To capture these effects in the constitutive model, for a N_l-layer strand, the proposed rheological model consists of a multiaxial spring system made of uniaxial spring systems assigned to a discrete set of directions, where each uniaxial spring system consists of a spring and N_l slider-springs. In a uniaxial spring system, the spring represents the slip contribution of all wires to the bending stiffness of the strand, while each slider-spring represents the stick contribution of each layer. A major advantage of the proposed scheme is its straightforward parameter identification, requiring only several monotonic uniaxial bendings under constant axial force. The proposed rheological model has been verified against the responses obtained from a mixed stress–strain driven computational homogenization through several numerical examples. These examples consist of complex uniaxial and biaxial load cases with variable tensile force. It has been shown that the proposed scheme not only predicts the response of the strand, but also provides helpful insight into the complex underlying mechanisms reflecting the occurrence of interlayer slip. By implementing the proposed rheological model as the constitutive law in a beam model, spiral strand simulations can be performed in a few seconds on a laptop, instead of a few hours or days on a supercomputer.

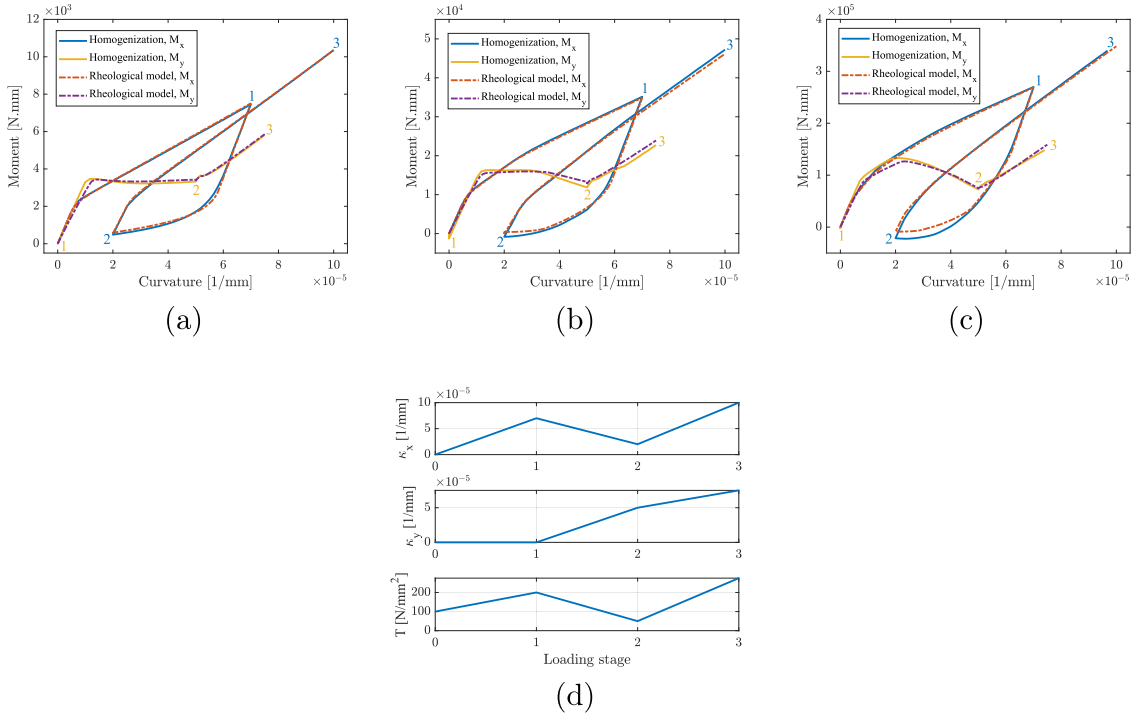

Fig. 28. A comparison of the bending responses in the *x*- and *y*-axes of spiral strands obtained from homogenization and from the rheological model for the biaxial test case 2 (the end of each load stage is marked on each curve). a, the single-layer strand; b, the two-layer strand; c, the four-layer strand; d, the loading history.

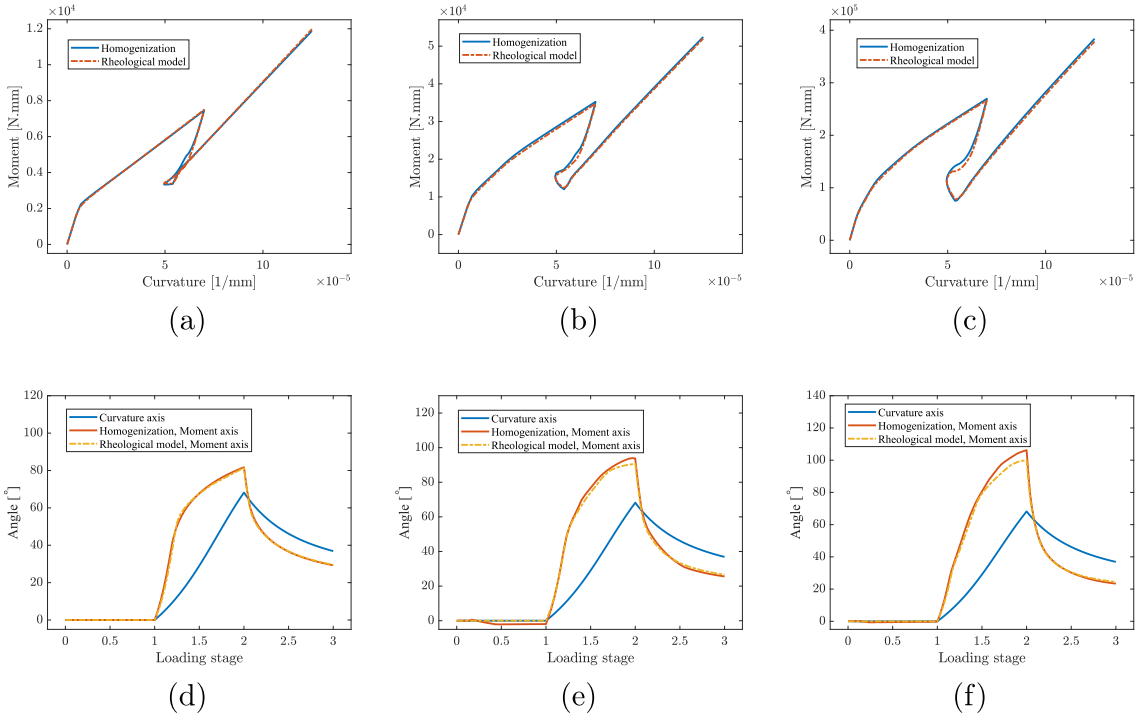

Fig. 29. A comparison of the bending response and the bending moment axis of spiral strands obtained from homogenization and from the rheological model for the biaxial test case 2. a,d, the single-layer strand; b,e, the two-layer strand; c,f, the four-layer strand.

CRediT authorship contribution statement

Mohammad Ali Saadat: Writing – review & editing, Writing – original draft, Visualization, Validation, Software, Methodology, Formal analysis, Conceptualization. **Damien Durville:** Writing – review & editing, Writing – original draft, Visualization, Validation, Supervision, Software, Methodology, Funding acquisition, Formal analysis, Conceptualization.

Declaration of competing interest

The authors declare that they have no known competing financial interests or personal relationships that could have appeared to influence the work reported in this paper.

Data availability

Data will be made available on request.

Acknowledgment and disclaimer

This work has received funding from the European Union's Horizon 2020 research and innovation programme under the Marie Skłodowska-Curie grant agreement No 860124. The present paper only reflects the authors' views. The European Commission and its Research Executive Agency are not responsible for any use that may be made of the information it contains.

References

Baumann, R., Novak, P., 2017. Efficient computation and experimental validation of ACSR overhead line conductors under tension and bending. CIGRE Sci. Eng. 9 (October), 5–16.
Beleznai, R., Páczelt, I., 2013. Design curve determination for two-layered wire rope strand using p-version finite element code. Eng. Comput. 29, 273–285.
Betsch, P., Steinmann, P., 2002. Frame-indifferent beam finite elements based upon the geometrically exact beam theory. Internat. J. Numer. Methods Engrg. 54 (12), 1775–1788.
Boso, D.P., Lefik, M., Schrefler, B.A., 2005. A multilevel homogenised model for superconducting strand thermomechanics. Cryogenics 45 (4), 259–271.
Bosten, A., Cosimo, A., Linn, J., Brüls, O., 2022. A mortar formulation for frictionless line-to-line beam contact. Multibody Syst. Dyn. 54 (1), 31–52.
Brüls, O., Cardona, A., Arnold, M., 2012. Lie group generalized-α time integration of constrained flexible multibody systems. Mech. Mach. Theory 48, 121–137.
Buannic, N., Cartraud, P., 2001. Higher-order effective modeling of periodic heterogeneous beams. I. Asymptotic expansion method. Int. J. Solids Struct. 38 (40–41), 7139–7161.
Bussolati, F., 2019. Modèle Multi-Échelle de la Fatigue des Lignes d'Ancrage Câblées pour l'Éolien Offshore Flottant (Ph.D. thesis). Université Paris-Saclay (ComUE).
Cardona, A., Geradin, M., 1988. A beam finite element non-linear theory with finite rotations. Internat. J. Numer. Methods Engrg. 26 (11), 2403–2438.
Cardou, A., 2013. Stick-Slip Mechanical Models for Overhead Electrical Conductors in Bending. GREMCA, Université Laval, Québec.
Cardou, A., Jolicoeur, C., 1997. Mechanical models of helical strands. Appl. Mech. Rev. 50 (1), 1–14.
Cartraud, P., Messager, T., 2006. Computational homogenization of periodic beam-like structures. Int. J. Solids Struct. 43 (3–4), 686–696.
Costello, G.A., 1997. Theory of Wire Rope. Springer Science & Business Media.
Costello, G.A., Butson, G.J., 1982. Simplified bending theory for wire rope. J. Eng. Mech. Div. 108 (2), 219–227.
Crisfield, M.A., Jelenić, G., 1999. Objectivity of strain measures in the geometrically exact three-dimensional beam theory and its finite-element implementation. Proc. R. Soc. Lond. Ser. A Math. Phys. Eng. Sci. 455 (1983), 1125–1147.
Dastous, J.-B., 2005. Nonlinear finite-element analysis of stranded conductors with variable bending stiffness using the tangent stiffness method. IEEE Trans. Power Deliv. 20 (1), 328–338.
Durville, D., 1998. Modélisation du comportement mécanique de câbles métalliques. Rev. Eur. Elem. Finis 7 (1–3), 9–22.
Durville, D., 2005. Numerical simulation of entangled materials mechanical properties. J. Mater. Sci. 40, 5941–5948.
Durville, D., 2010. Simulation of the mechanical behaviour of woven fabrics at the scale of fibers. Int. J. Mater. Form. 3, 1241–1251.
Durville, D., 2012. Contact-friction modeling within elastic beam assemblies: an application to knot tightening. Comput. Mech. 49 (6), 687–707.
Feyel, F., Chaboche, J.-L., 2000. FE2 multiscale approach for modelling the elasto-viscoplastic behaviour of long fibre SiC/Ti composite materials. Comput. Methods Appl. Mech. Engrg. 183 (3–4), 309–330.
Foti, F., Martinelli, L., 2016a. An analytical approach to model the hysteretic bending behavior of spiral strands. Appl. Math. Model. 40 (13–14), 6451–6467.
Foti, F., Martinelli, L., 2016b. Mechanical modeling of metallic strands subjected to tension, torsion and bending. Int. J. Solids Struct. 91, 1–17.
Frikha, A., Cartraud, P., Treyssede, F., 2013. Mechanical modeling of helical structures accounting for translational invariance. Part 1: Static behavior. Int. J. Solids Struct. 50 (9), 1373–1382.
Ghosh, S., Roy, D., 2009. A frame-invariant scheme for the geometrically exact beam using rotation vector parametrization. Comput. Mech. 44, 103–118.
Hong, K.-J., Der Kiureghian, A., Sackman, J.L., 2005. Bending behavior of helically wrapped cables. J. Eng. Mech. 131 (5), 500–511.
Hong, K.-J., Yi, C., Lee, Y.-k., 2012. Geometry and friction of helically wrapped wires in a cable subjected to tension and bending. Int. J. Steel Struct. 12 (2), 233–242.
Inagaki, K., Ekh, J., Zahrai, S., 2007. Mechanical analysis of second order helical structure in electrical cable. Int. J. Solids Struct. 44 (5), 1657–1679.
Inc., W.R., 2023. Mathematica, Version 13.3. Champaign, IL, URL: https://www.wolfram.com/mathematica.
Jiang, W.-G., 2012. A concise finite element model for pure bending analysis of simple wire strand. Int. J. Mech. Sci. 54 (1), 69–73.
Karathanasopoulos, N., Kress, G., 2016. Two dimensional modeling of helical structures, an application to simple strands. Comput. Struct. 174, 79–84.
Khan, S.W., Gencturk, B., Shahzada, K., Ullah, A., 2018. Bending behavior of axially preloaded multilayered spiral strands. J. Eng. Mech. 144 (12), 04018112.
Kim, S.-Y., Lee, P.-S., 2017. Modeling of helically stranded cables using multiple beam finite elements and its application to torque balance design. Constr. Build. Mater. 151, 591–606.
Kim, H.-J., Lee, D.-H., Yoon, K., Lee, P.-S., 2021. A multi-director continuum beam finite element for efficient analysis of multi-layer strand cables. Comput. Struct. 256, 106621.
Kmet, S., Stanova, E., Fedorko, G., Fabian, M., Brodniansky, J., 2013. Experimental investigation and finite element analysis of a four-layered spiral strand bent over a curved support. Eng. Struct. 57, 475–483.
Lalonde, S., Guilbault, R., Langlois, S., 2017a. Modeling multilayered wire strands, a strategy based on 3D finite element beam-to-beam contacts-Part II: Application to wind-induced vibration and fatigue analysis of overhead conductors. Int. J. Mech. Sci. 126, 297–307.
Lalonde, S., Guilbault, R., Légeron, F., 2017b. Modeling multilayered wire strands, a strategy based on 3D finite element beam-to-beam contacts-Part I: Model formulation and validation. Int. J. Mech. Sci. 126, 281–296.
Lanteigne, J., 1985. Theoretical estimation of the response of helically armored cables to tension, torsion, and bending. J. Appl. Mech. 52 (2), 423–432.
LeClair, R.A., Costello, G.A., 1988. Axial, bending and torsional loading of a strand with friction. J. Offshore Mech. Arct. Eng. 110 (1), 38–42.
Love, A.E.H., 1927. A Treatise on the Mathematical Theory of Elasticity. University Press.
Matouš, K., Geers, M.G., Kouznetsova, V.G., Gillman, A., 2017. A review of predictive nonlinear theories for multiscale modeling of heterogeneous materials. J. Comput. Phys. 330, 192–220.
Meier, C., Grill, M.J., Wall, W.A., Popp, A., 2018. Geometrically exact beam elements and smooth contact schemes for the modeling of fiber-based materials and structures. Int. J. Solids Struct. 154, 124–146.
Meier, C., Popp, A., Wall, W.A., 2015. A locking-free finite element formulation and reduced models for geometrically exact Kirchhoff rods. Comput. Methods Appl. Mech. Engrg. 290, 314–341.
Ménard, F., Cartraud, P., 2021. Solid and 3D beam finite element models for the nonlinear elastic analysis of helical strands within a computational homogenization framework. Comput. Struct. 257, 106675.
Miehe, C., Göktepe, S., Lulei, F., 2004. A micro-macro approach to rubber-like materials—part I: the non-affine micro-sphere model of rubber elasticity. J. Mech. Phys. Solids 52 (11), 2617–2660.
Moustacas, H., Wielhorski, Y., Durville, D., 2021. Higher order beam model with appropriate constitutive model for the modelling of carbon fiber tows. In: 14-th WCCM&ECCOMAS Congress 2020.
Papailiou, K.O., 1995. Bending of Helically Twisted Cables Under Variable Bending Stiffness Due to Internal Friction, Tensile Force and Cable Curvature (Doctor of Technical Sciences thesis). ETH, Athens, Greece.
Papailiou, K., 1997. On the bending stiffness of transmission line conductors. IEEE Trans. Power Deliv. 12 (4), 1576–1588.
Paradis, J.-P.H., Légeron, F., 2011. Modelling of the free bending behavior of a multilayer cable taking into account the tangential compliance of contact interfaces. In: Ninth International Symposium on Cable Dynamics. pp. 18–20.
Ramsey, H., 1988. A theory of thin rods with application to helical constituent wires in cables. Int. J. Mech. Sci. 30 (8), 559–570.
Rega, G., 2004a. Nonlinear vibrations of suspended cables—Part I: Modeling and analysis. Appl. Mech. Rev. 57 (6), 443–478.
Rega, G., 2004b. Nonlinear vibrations of suspended cables—part II: deterministic phenomena. Appl. Mech. Rev. 57 (6), 479–514.

Reissner, E., 1973. On one-dimensional large-displacement finite-strain beam theory. Stud. Appl. Math. 52 (2), 87–95.
Saadat, M.A., Durville, D., 2023. A mixed stress-strain driven computational homogenization of spiral strands. Comput. Struct. 279, 106981.
Simo, J.C., 1985. A finite strain beam formulation. The three-dimensional dynamic problem. Part I. Comput. Methods Appl. Mech. Engrg. 49 (1), 55–70.
Smith, D.M., Cunningham, L.S., Chen, L., 2023. Efficient finite element modelling of helical strand cables utilising periodicity. Int. J. Mech. Sci. 108792.
Sonneville, V., Cardona, A., Brüls, O., 2014. Geometrically exact beam finite element formulated on the special Euclidean group SE (3). Comput. Methods Appl. Mech. Engrg. 268, 451–474.
Starossek, U., 1994. Cable dynamics-a review. Struct. Eng. Int. 4 (3), 171–176.
Staszak, N., Gajewski, T., Garbowski, T., 2022. Shell-to-beam numerical homogenization of 3D thin-walled perforated beams. Materials 15 (5), 1827.
Tomec, J., Jelenić, G., 2022. Analysis of static frictionless beam-to-beam contact using mortar method. Multibody Syst. Dyn. 55 (3), 293–322.
Treyssede, F., Cartraud, P., 2022. A two-dimensional formulation for the homogenization of helical beam-like structures under bending loads. Int. J. Solids Struct. 234, 111270.
Triantafyllou, M., 1984. Linear dynamics of cables and chains. Shock Vib. Dig. 16 (3), 9–17.
Utting, W., Jones, N., 1984. A survey of literature on the behaviour of wire ropes. Wire Ind. 51 (609), 623–629.
Vemula, S.S., Ji, M., Headings, L.M., Gargesh, K., Soghrati, S., Dapino, M.J., 2020. Analytical model for large deflection bending of helically stranded electrical wires. Int. J. Mech. Sci. 170, 105355.
Wriggers, P., Laursen, T.A., 2006. Computational Contact Mechanics, vol. 2, Springer.
Wriggers, P., Zavarise, G., 1997. On contact between three-dimensional beams undergoing large deflections. Commun. Numer. Methods Eng. 13 (6), 429–438.
Xing, Y., Meng, L., Huang, Z., Gao, Y., 2022. A novel efficient prediction method for microscopic stresses of periodic beam-like structures. Aerospace 9 (10), 553.
Yu, Y., Chen, Z., Liu, H., Wang, X., 2014. Finite element study of behavior and interface force conditions of seven-wire strand under axial and lateral loading. Constr. Build. Mater. 66, 10–18.
Yu, Y., Wang, X., Chen, Z., 2016. A simplified finite element model for structural cable bending mechanism. Int. J. Mech. Sci. 113, 196–210.
Yu, C., Yin, S., Dong, B., Bao, Y., 2018. The analysis of 91-wire strand tensile behavior using beam finite element model. In: IOP Conference Series: Materials Science and Engineering, vol. 381, IOP Publishing, 012115.
Zavarise, G., Wriggers, P., 2000. Contact with friction between beams in 3-D space. Internat. J. Numer. Methods Engrg. 49 (8), 977–1006.
Zhang, D., Ostoja-Starzewski, M., 2016. Finite element solutions to the bending stiffness of a single-layered helically wound cable with internal friction. J. Appl. Mech. 83 (3).
Zheng, X., Hu, Y., Zhou, B., Li, J., 2021. Modelling of the hysteretic bending behavior for helical strands under multi-axial loads. Appl. Math. Model. 97, 536–558.
Zhou, B., Hu, Y., Zheng, X., Zhu, H., 2022. Bending behavior of a frictional single-layered spiral strand subjected to multi-axial loads: Numerical and experimental investigation. Appl. Sci. 12 (9), 4792.
Zhou, W., Tian, H.-q., 2013. A novel finite element model for single-layered wire strand. J. Cent. South Univ. 20 (6), 1767–1771.